True-to-scale DNA-density maps correlate with major accessibility differences between active and inactive chromatin

Márton Gelléri[1*+], Shi-Ya Chen[1*], Aleksander Szczurek[1a], Barbara Hübner[2b]
Michael Sterr[2c], Jan Neumann[1,3d], Ole Kröger[4], Filip Sadlo[4], Jorg Imhoff[5],
Yolanda Markaki[2e], Michael J. Hendzel[6], Marion Cremer[2], Thomas Cremer[2],
Hilmar Strickfaden[1,6+], Christoph Cremer[1,3,4,7+]

1.) Institute of Molecular Biology (IMB), Mainz, Germany

2.) Biocenter, Dept Biology II, Ludwig Maximilian University (LMU), Munich, Germany)

3.) Max Planck Institute for Chemistry, Mainz, Germany

4.) Interdisciplinary Center for Scientific Computing (IWR), University Heidelberg, Heidelberg, Germany

5.) Neuroconsult GmbH, Heidelberg, Germany

6.) Department of Oncology, Cross Cancer Institute, University of Alberta, Edmonton, Alberta, Canada

7.) Kirchhoff Institute of Physics, University Heidelberg, Heidelberg, Germany

*equal contributions

[a]AS, present address: Department of Biochemistry, Oxford University, Oxford, UK
[b]BH, present address: Nanyang Technological University, School of Biological Sciences & NTU Institute of Structural Biology (NISB), Singapore
[c]MS, present address: Helmholtz Center Munich, Institute of Diabetes and Regeneration Research (IDR), Neuherberg, Germany
[d]JN, present address: SAP AG, Walldorf, Germany
[e]YM, present address: Department of Biological Chemistry, David Geffen School of Medicine, University of California, Los Angeles, CA 90095, USA

+corresponding authors:
Christoph Cremer: C.Cremer@imb-mainz.de
Márton Gelléri: M.Gelleri@imb-mainz.de
Hilmar Strickfaden: hilmar@ualberta.ca; hilmar@structural-epigenetics.org

Short title:
High-resolution nuclear DNA density maps

One-sentence summary
Super-resolved DNA density maps and nanobead microinjection experiments support major compaction and accessibility differences between active and inactive chromatin compartments

Keywords: active and inactive nuclear compartments (ANC and INC), true-to-scale DNA density maps (Mbp/µm^3), microinjected nanobeads, replication domains (RDs), single molecule localization microscopy (SMLM), structured illumination microscopy (SIM), electron spectroscopic imaging (ESI), quantitative image analysis, Voronoi-tessellation

Abstract

Chromatin compaction differences may have a strong impact on accessibility of individual macromolecules and macromolecular assemblies to their DNA target sites. Estimates based on fluorescence microscopy with conventional resolution, however, suggested only modest compaction differences (~2-10x) between active and inactive nuclear compartments (ANC and INC). Here, we present maps of nuclear landscapes with true-to-scale DNA-densities, ranging from <5 Mbp/μm^3 to >300 Mbp/μm^3. Maps were generated from individual human and mouse cell nuclei with single-molecule localization microscopy at ~20 nm lateral and ~100 nm axial resolution and supplemented by electron spectroscopic imaging. Live cell microinjection experiments with 20 nm and 40 nm sized fluorescent beads, corresponding to macromolecular assemblies for transcription and replication, indicated movements within the ANC, but exclusion from the INC. In line with previous studies of transcription, pulse-chase labeling experiments of DNA demonstrated replication within the ANC, followed by re-location of replicated, inactive chromatin into the INC.

Introduction

Understanding the functional behavior of genomes requires knowledge of the dynamic biochemical and physical chromatin loop organization[1] and its consequences for the accessibility of individual macromolecules, condensates with proteins and RNAs, as well as of structured macromolecular assemblies involved in nuclear functions. Microscopic studies of nuclear architecture have provided evidence for a multitude of chromatin ensembles with chromatin domains (CDs) and chromosome territories (CTs), as well as for a functional nuclear organization based on active and inactive nuclear compartments (ANC/INC)[2-5]. Chromatin ensembles, such as topologically associating domains (TADs) and A- and B-compartments, were independently

identified by genome wide measurements of 3D chromatin contacts[6-9] (for a glossary of currently used nomenclatures and conceptual differences, see supplemental information in[10]). Physical maps of nuclear landscapes, supplemented with biochemical information about epigenetic markers and attachment sites of specific macromolecules and functional complexes, have revolutionized our views on nuclear organization. How nuclear compartments are established and maintained, and how they interact functionally, has remained a largely unsolved problem[11,12]. Higher order chromatin arrangements differ substantially not only between different cell types and species, but also from cell to cell of a given cell population of the same cell type[5,13]. This heterogeneity may reflect in part functionally irrelevant stochastic features of 4D spatial genomics, while other features, including the space-time organization of nuclear landscapes at mesoscale, reflect a functionally indispensable preciseness of genome organization[14,15] (see Discussion).

In this study, we deal with the important, still unresolved problem of true-to-scale compaction levels of chromatin ensembles, constituting active and inactive nuclear compartments, and their different accessibility for individual functional macromolecules and macromolecular aggregates, such as transcription-, replication- and repair machineries. At face value, a large body of evidence obtained in previous studies suggests only modest compaction and accessibility differences between active and inactive chromatin ensembles. Our present study challenges this concept.

Figure 1a-b shows views of higher order chromatin organization based on apparently ‘open’ chromatin loop configurations. Accordingly, an interchromatin space expanding both within the interior and outside of individual loops seems wide enough to allow penetration of individual macromolecules and complete macromolecular machineries (Figure 1c). In contrast, concepts of a much more ‘crumpled’ organization of chromatin (Figure 1d), and a ‘closed’ configuration of densely packaged

nucleosomes (Figure 1e), may constrain the penetration of individual macromolecules into the interior of chromatin ensembles, and exclude the penetration of macromolecular machineries or phase-separated condensates[16]. Our current version of the ANC-INC model (Figure 1f) supports this concept[2] (see below).

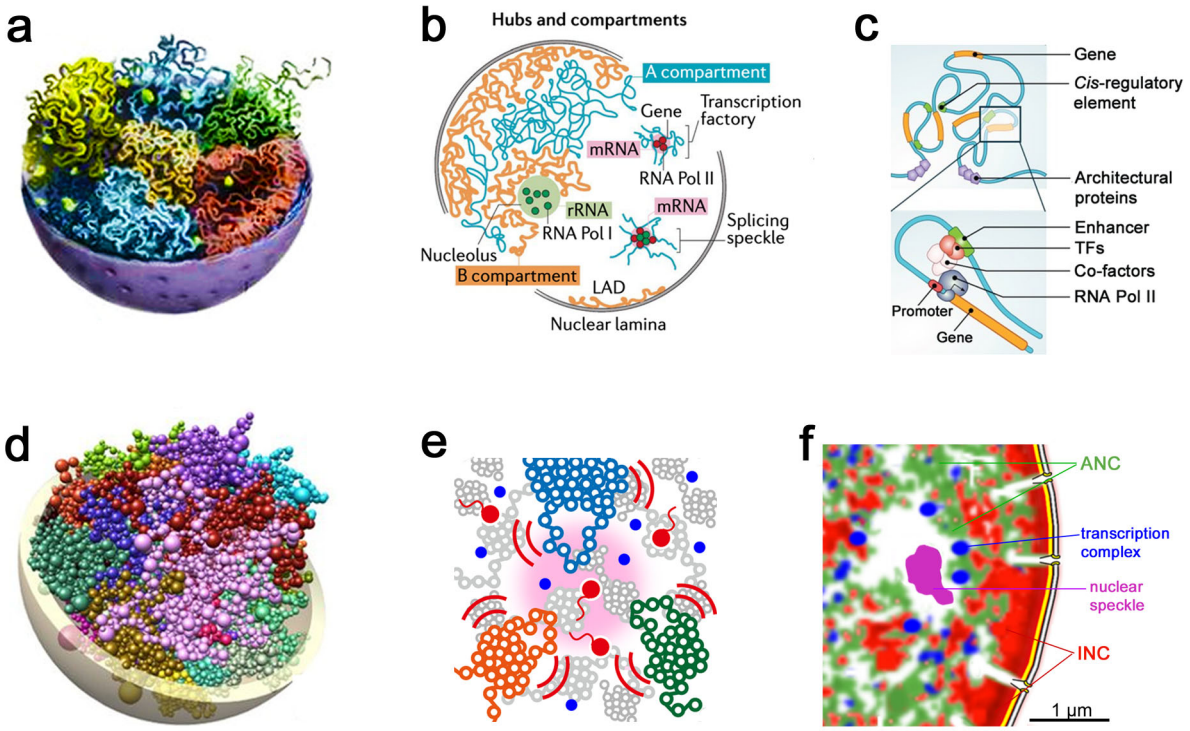

Figure 1: Views of 3D nuclear landscape

Current views of nuclear organisation at mesoscale agree that chromosomes occupy distinct territories (CTs)/domains[3,6-9,17,18]. Current concepts of chromatin compaction, however, range from relatively open chromatin loop configurations ***a***[6]*;* ***b***[8]*;* ***c***[9] *to proposals as in* ***d*** *describing the crumpled organization of chromatin as little balls without giving an opinion on the density of chromatin inside[18].* ***e*** *Higher order chromatin organization of chromatin based on nucleosome clusters (NCs)[19]. Red dots: RNAPII; blue dots: transcription factors. NCs may form the first level of higher order chromatin structures beyond individual nucleosomes[20].* ***f*** *ANC-INC model of nuclear architecture[2,3]. The active nuclear compartment (ANC) comprises the Interchromatin compartment (IC). IC-channels start at nuclear pores. The IC forms a network throughout the nuclear interior and expands at certain sites into wider IC-lacunae, which carry splicing speckles and other nuclear bodies. It is lined by the perichromatin region (PR) with less dense and more accessible chromatin (green). The inactive nuclear compartment (INC) carries more compact and poorly accessible chromatin (red); for further details see Figure 7 and text.*

It is of note that many published cartoons show details of nuclear landscapes that are not drawn to scale. Such cartoons may suggest that scale is not an important issue. The dynamic, true-to-scale spatial chromatin compaction, however, is a fundamental issue of chromatin accessibility with major functional implications for co-

125 aligned active and inactive chromatin ensembles (see Discussion). This problem
126 cannot be solved solely by studies based on 3D DNA contact frequencies, but requires
127 true-to-scale, high-resolution maps across entire nuclear landscapes obtained by
128 microscopy with super-resolution. Studies performed with the resolution limit of
129 conventional fluorescence microscopy (~200 nm in the object plane, and ~600 nm
130 along the optical axis), have suggested relatively small density differences between
131 euchromatin and heterochromatin regions, and underestimated the true density related
132 differences between 'open' and 'closed' chromatin (e.g.[21-23]), comparable to a
133 landscape of a mountain region, recorded from an airplane with a poor resolution
134 camera, that levels the differences between high mountains and deep valleys.
135 Estimates of absolute nucleosome densities in live HeLa cell nuclei, obtained by a
136 combination of Fluorescence Correlation Spectroscopy and Confocal Imaging[24],
137 revealed about tenfold intranuclear differences in local nucleosome density, ranging
138 from about 25 μM to 250 μM. Assuming 200 bp per nucleosome (including linker DNA),
139 these values amount to about 3 Mbp/μm^3 for low density regions and 30 Mbp/μm^3 for
140 high density regions. The authors have argued that a nucleosome density of 250 μM
141 would not be sufficient to create an accessibility barrier for diffusing protein complexes
142 from euchromatin into heterochromatin, but mentioned that they could not exclude the
143 possibility of the formation of local barriers only detectable with a much higher
144 structural resolution.

145 A study of nuclei in live-murine cells performed with laser confocal microscopy
146 by Maeshima and colleagues[25] revealed a 7.5-fold higher intensity of Hoechst-stained
147 DNA in heterochromatic foci compared to surrounding euchromatic regions. In
148 addition, with differential interference contrast microscopy the authors observed a 1.5-
149 fold difference of dry mass densities between heterochromatin (208 mg/ml) and
150 euchromatin (136 mg/ml). Based on Monte Carlo simulations, the authors suggested

151 that this difference contributes to a moderate access barrier of non-nucleosomal
152 materials (proteins/RNAs) that constrains the diffusion of proteins into
153 heterochromatin.

154 Whereas studies with conventional optical resolution comprises an observation
155 volume in the order of ~10,000 nucleosomes[24], the improved structural resolution
156 obtained with single molecule localization microscopy (SMLM) (for reviews see[26-30])
157 allows the visualization of individual clusters with less than 100 nucleosomes. Previous
158 microscopic studies performed at this highly enhanced resolution level have indicated
159 dense assemblies of nucleosomes in heterogeneous groups comprising a few kb of
160 DNA, termed nucleosome clutches (NCs)[20]. NCs provide candidate structures that
161 may represent building blocks for all higher-order nucleosome structures above the
162 single nucleosome level, such as chromatin domains or TAD-like structures[20,31-33].

163 The present quantitative, high-resolution study presents the first true-to-scale
164 3D DNA density maps of the absolute heights of DNA density peaks and valleys across
165 entire nuclear landscapes of individual cells in terms of Mbp/μm^3 at nanometer-scale
166 resolution. Differences between high density chromatin structures assigned to the INC
167 and low DNA density regions assigned to the ANC[2,19] range from <5 Mbp/μm^3 to >300
168 Mbp/μm^3 and are much larger than DNA compaction differences claimed in previous
169 studies with conventional microscopic resolution. In addition, we performed
170 microinjection experiments with 20 nm and 40 nm sized fluorescent nanobeads,
171 reflecting sizes of macromolecular assemblies for transcription and replication, and
172 demonstrate their enrichment in the active nuclear compartment (ANC) and exclusion
173 from the inactive compartment (INC). These findings support a substantially lower
174 compaction in the ANC associated with a higher accessibility of chromatin ensembles
175 compared to the INC, with major implications for the functional organization of the cell
176 nucleus. For a glimpse on dynamic functional interactions between co-aligned ANC

177 and INC chromatin ensembles, we conducted DNA pulse labeling experiments during
178 S-phase, demonstrating replication of both early-replicating euchromatin and mid-late
179 replicating heterochromatic blocks within the ANC. Pulse-chase labeling experiments
180 of constitutive heterochromatin blocks revealed the re-location of replicated, inactive
181 chromatin into dense chromatin attributed to the INC.

182

183 **Results**

184 **Determination of absolute DNA densities across nuclear landscapes**

185 Single Molecule Localization Microscopy (SMLM)[34] combined with fluctuation-assisted
186 Binding Activated Localization Microscopy (fBALM)[35,36] was used to record millions of
187 blinking events of the fluorophore Sytox Orange, bound to double-stranded DNA in
188 single light optical sections from human and mouse fibroblasts and from HeLa, as an
189 example of a human cancer cell-line.

190 Figure 2 presents the color-coded, Voronoi-tessellated true-to-scale 3D DNA
191 density SMLM-fBALM image obtained from a mid-plane optical section through a
192 human fibroblast nucleus (BJ1) in G1 stage of the cell cycle (Figure 2a). This image
193 was generated from ~1.5 million spatially mapped blinking events, registered in 50,000
194 consecutively recorded frames. Single Molecule Positions (SMPs) of these events
195 were located within an optical section of about 100 nm thickness with an average
196 localization precision of ~50 nm along the optical axis and an average lateral
197 localization precision of ca. 8 nm (for details of this procedure see Methods and
198 Supplemental Figure S1). Figures 2b, c (upper panel) show selected regions with
199 increasing magnifications. For panels a-c, a color-coded scale bar for 3D DNA
200 densities with emphasis on the range >5 Mbp/μm^3 and <40 Mbp/μm^3 is presented at
201 top of Figure 2b. Figure 2c (lower panel) presents the Voronoi tesselations used for
202 reconstructions of images 2c (upper panel). Figure 2d presents the same panel shown

203 in Figure 2c with another color-bar code (below) that emphasizes the range of 3D DNA
204 densities from >40 Mbp/μm^3 up to ~350 Mbp/μm^3.
205 Absolute DNA densities (Mbp/μm^3) were calculated as follows: In addition to the
206 total number of SMPs, we estimated both the volume, comprising about 1/20th of the
207 nuclear volume, and the total DNA content of the 100 nm thick optical section. From
208 these numbers, we calculated that a single SMP in this BJ1 nucleus was representative
209 on average for about 200 bp, that is roughly the DNA surrounding a single nucleosome
210 (see Methods for further details). Next, we used 2D Voronoi-tessellation[37] for
211 partitioning 2D SMP density images into 2D polygonal images. Assuming that each 2D
212 polygon represents in fact a 3D polygonal prism with a depth of 100 nm, we calculated
213 the average DNA density for each prism by dividing its DNA content (based on the
214 number of SMPs) by its volume. Polygonal Voronoi prisms were color-coded
215 corresponding to 3D DNA density estimates, ranging from <5 Mbp/μm^3 (white) to >40
216 Mbp/μm^3 (deep red), respectively, as indicated in the color-coded scale for 2a-c. A
217 further unfolding of color codes for densities >40 Mbp/μm^3 up to ~350 Mbp/μm^3 and
218 corresponding SMP densities is provided in the color scale column in Figure 2d.

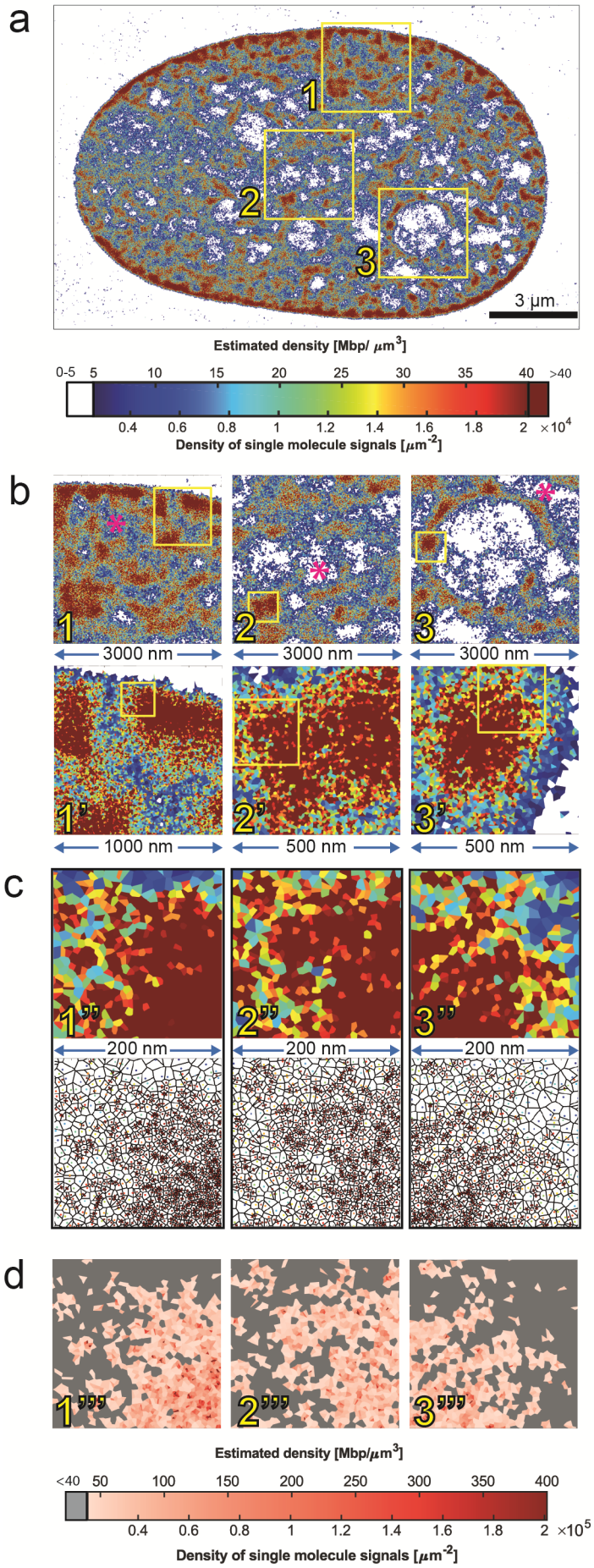
a
1
2
3
3 µm
Estimated density [Mbp/ µm3]
0-5 5 10 15 20 25 30 35 40 >40
0.4 0.6 0.8 1 1.2 1.4 1.6 1.8 2 ×10^4
Density of single molecule signals [µm-2]
b
1
2
3
3000 nm
3000 nm
3000 nm
1'
2'
3'
1000 nm
500 nm
500 nm
c
1''
2''
3''
200 nm
200 nm
200 nm
d
1'''
2'''
3'''
Estimated density [Mbp/µm3]
<40 50 100 150 200 250 300 350 400
0.4 0.6 0.8 1 1.2 1.4 1.6 1.8 2 ×10^5
Density of single molecule signals [µm-2]

219

Figure 2: High-resolution, true-to-scale DNA density landscape of human fibroblast nucleus

a *Voronoi-tessellated SMLM-fBALM image of a mid-optical section (thickness ~100 nm through a diploid human fibroblast cell nucleus (BJ1) stained with Sytox Orange (see Methods for further explanation how this image was generated). The color code indicates the estimated range of 3D DNA densities from <5 Mbp/µm^3 to >40 Mbp/µm^3, reflecting 2D SMP densities <2,500 SMPs/µm^2 to >20,000 SMPs/µm^2 (see Supplemental Figure S1 and Results for 3D DNA densities estimated from 2D SMP densities in 100 nm thick sections).* ***b, 1-3*** *Magnifications of the three boxed areas in (a) demonstrate sites located at the nuclear periphery (1) and in the nuclear interior (2, 3); edge length 3000 nm. Asterisks denote IC-lacunae.* ***b, 1'–3'*** *Further magnification of boxed areas in (1-3), edge lengths 1000 nm (1'), and 500 nm (2',3').* ***c, 1''–3''*** *upper row: Further magnification of boxed areas in (1'-3'), edge length 200 nm. lower row: Individual Voronoi centers (seeds) are shown for the same Voronoi areas as in 1'' – 3''.* ***d, 1'''–3'''*** *same areas as in c 1'' depicted here with another color code (shown at bottom) for 3D DNA densities from 40 Mbp/µm^3 to about 350 Mbp/µm^3, reflecting a range of 2D SMP densities between ~20,000 and ~180,000 SMPs/µm^2.*

Figure 3 shows a color-coded, Voronoi-tessellated SMLM-fBALM image of a mid-optical nuclear section recorded from a HeLa cell nucleus, as an example of an aneuploid cancer cell with a near triploid genome content. Since here image recording was performed without an astigmatic lens placed in the optical path, the thickness of the optical section was about 600 nm. Within this optical section, Sytox Orange molecules were registered in 25,000 consecutive frames yielding about 4 million SMPs with an average lateral localization precision of ca. 12 nm. Compared to the ~20 nm lateral resolution achieved for the BJ1 nucleus (Figure 2), the lateral structural resolution achieved for this HeLa nuclear landscape was slightly reduced (~30 nm) due to the lesser overall density of SMPs and a somewhat smaller localization precision[34]. True-to-scale DNA density estimates were calculated and ranged between <5 Mbp/µm^3 and >150 Mbp/µm^3, considering a triploid DNA content and the assumption of G1 stage for an assessment of the minimum density range. Note that these estimates would increase by a factor 2 in case of a G2 DNA content. Especially at the nuclear periphery, we noted ensembles of high-density peaks with diameters up to several hundreds of nm, surrounded by chromatin with lower densities.

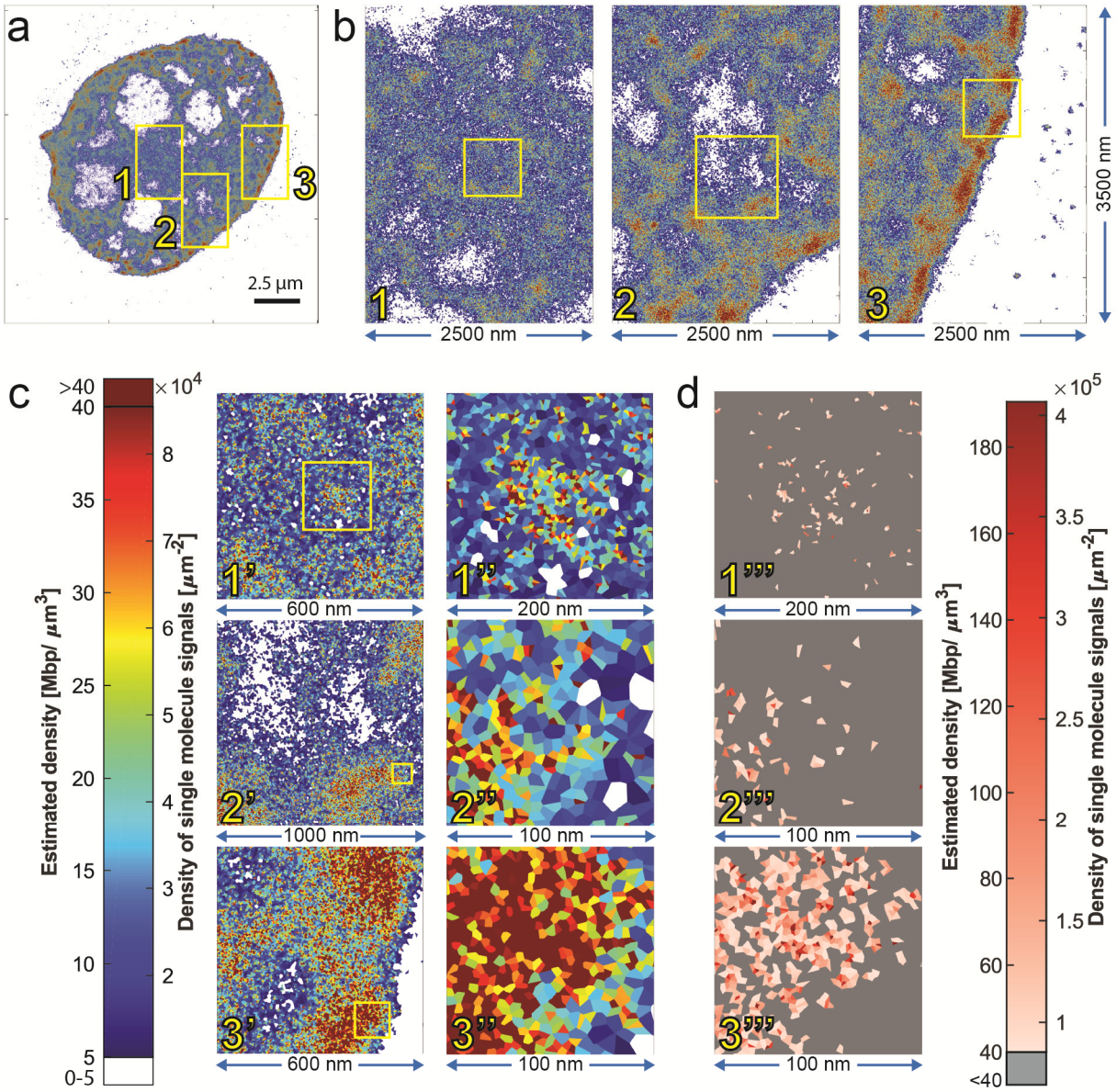

254
255 **Figure 3: High-resolution, true-to-scale DNA density landscape of a HeLa cell**
256 **nucleus**
257 ***a*** *SMLM-fBALM image (Voronoi-tessellation) of a mid-optical section (thickness ~600 nm)*
258 *through a HeLa cell nucleus.* ***b, 1-3*** *Magnifications of the three boxed areas in (a); edge lengths*
259 *2.5 µm x 3.5 µm.* ***c*** *The color code shown on the left presents (right side of the column) the*
260 *density of blinking signals (up to >8x10⁴ SMPs/µm²) recorded from DNA-bound Sytox Orange*
261 *fluorophores (SMPs) and (left side of this column) the estimated absolute densities (Mbp/µm³)*
262 *between <5 Mbp/µm³ and >40Mbp/µm³; this color code is valid for all images in a-c.* ***c, 1'-3'***
263 *Further magnification of boxed areas in (b,1-3); edge length 600 nm(1'), 1 µm (2'), and 600 nm*
264 *(3'), respectively.* ***c, 1''-3''*** *Further magnification of boxed areas in c,1'- 3'; edge length 200 nm*
265 *(1'') and 100 nm in (2'') and (3''), respectively.* ***d, 1'''- 3'''*** *The same regions as in c,1''- 3'' show*
266 *the individual Voronoi cells with apparent DNA densities above 40 Mbp/µm³; edge length 200*
267 *nm (1''') and 100 nm (2''', 3'''), respectively; the color code in (d) (right column) presents the*
268 *signal densities of SMPs (up to >4 x 10⁵/µm²) and the estimated absolute densities (Mbp/µm³)*
269 *between 40 Mbp/µm³ and 190 Mbp/µm³.*
270

In summary, Figures 2 and 3 exemplify the potential of our approach to identify the true-to-scale topography and widely different 3D DNA densities of chromatin ensembles across entire nuclear landscapes from mesoscale to the nanoscale.

Figure 4 shows a comparison of the DNA landscapes of a mouse C3H 10T1/2 fibroblast nucleus obtained from a Voronoi-tessellated SMLM-fBALM image (Figure 4a) and electron spectroscopic imaging (ESI)[38] (Figure 4b-e) with the same thickness (100 nm) of light optical and physical ultra-thin midsections, respectively. The two mouse fibroblast nuclei vary with regard to the more expanded IC (blue) in the nucleus studied with ESI; apart from this their DNA-density landscapes appear remarkably similar with less dense chromatin in the PR. In both human and mouse nuclei we note an enrichment of highly compact DNA at the nuclear periphery. In contrast to the human fibroblast nucleus, the mouse fibroblast nucleus carries prominent clusters of constitutive heterochromatin, called chromocenters (depicted by arrows).

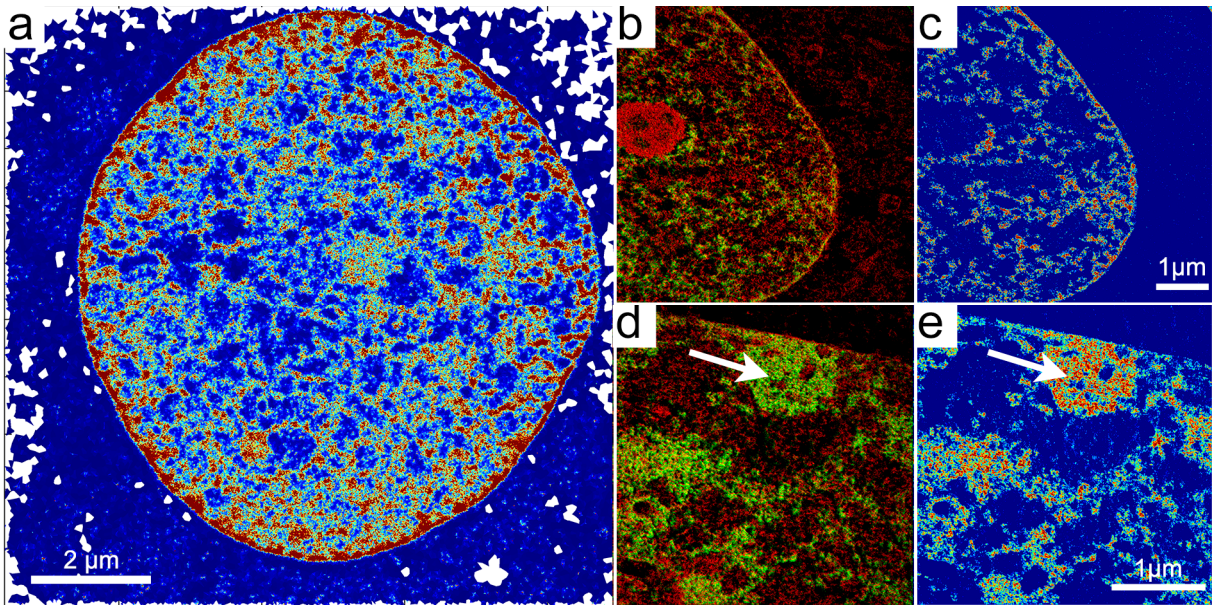

Figure 4: Comparison of high-resolution DNA landscapes of mouse C3H T1/2 fibroblast nuclei recorded with SMLM and ESI

a *100 nm optical mid-section through a mouse C3H T1/2 fibroblast nucleus recorded with SMLM-fBALM.* ***b-e*** *ESI micrographs taken from acrylic 100 nm thin mid-sections through another C3H T1/2 fibroblast nucleus.* ***b*** *and* ***d*** *show superimposed elemental maps of phosphorus (green) and nitrogen (red).* ***c*** *and* ***e*** *present the phosphorus map only, color-coded for different phosphorus densities as a reflection of DNA densities. For better comparison, the same color-coded look-up table (jet) was used for SMLM (a) and ESI images (c,e; blue indicates lowest DNA densities that belong to the IC, lined by light blue and green colored*

intermediate densities (PR); red marks high DNA compaction attributed to the INC (compare Figures 2 and 3). Arrows in (d) and (e) indicate examples of chromocenters. In order to secure that only the DNA landscape was recorded, RNA was digested in both nuclei prior to imaging.

Localization and constrained movements of microinjected nanobeads within the ANC

Evidence presented above supports DNA density differences, ranging from <5 Mbp/μm^3 in the ANC to >300 Mbp/μm^3 in the INC. For a rough idea of mechanical accessibility barriers imposed by chromatin, we estimated 3D distances between the surfaces of nucleosomes, represented by 10 nm sized spheres uniformly arranged in 3D space in comparison to a spherical protein with 5 nm diameter, and a 20 nm sized condensate or macromolecular machinery. We assumed DNA fully packaged with nucleosomes at different DNA densities of 5, 30, 60 and 150 Mbp/μm^3 (Figure 5a). At face value, Figure 5a favors the hypothesis of an accessibility barrier of dense nucleosome aggregates attributed to the INC. Apparently, there is little room left for different geometrical arrangements of nucleosomes at very high DNA densities. On the contrary, geometrical nucleosome arrangements at low densities (<5 Mbp/μm^3) provide sufficient nucleosome free space for a variety of individual loop structures, which allow a high degree of accessibility for macromolecules and macromolecular complexes/condensates. Since the space-time dynamics of chromatin domains in nuclei of living cells is currently not well understood (see Discussion), it is not possible to conclude from the observed DNA density differences in fixed cell nuclei, to which extent chromatin in the INC with high compaction levels may constrain the accessibility of individual proteins and RNAs or fully exclude macromolecular machineries and condensates, assembled within the ANC. For an experimental test, we microinjected fluorescent beads with 20 nm and 40 nm diameter, respectively, into nuclei of living HeLa cells (Figure 5b-e) and of C3H 10T1/2 cells (Figure 5f-i). The sizes of these

321 nanobeads were chosen to approximate sizes of transcription-, and replication-
322 machineries or phase-separated droplets. HeLa cells used for microinjection
323 experiments were either kept in isotonic (290 mOsm) medium (Figure 5b), or in
324 hypertonic (570 mOsm) medium (Figure 5c), resulting in the rapid induction (~1 min)
325 of hyper-condensed chromatin (HCC). When cells with HCC were re-incubated in
326 medium with physiological osmolarity (290 mOsm) nuclei with normally condensed
327 chromatin (NNC) were quickly restored, even after several NNC-HCC-NCC cycles[39].
328 For both states of chromatin compaction, analysis of nanobead positions in fixed cell
329 nuclei demonstrated their presence in less condensed chromatin attributed to the ANC
330 (Figure 5d, e). Corresponding DNA (DAPI) intensity profiles are shown by line scans
331 through nuclei encompassing the site of a nanobead (Supplemental Figures S2 and
332 S3). Most HeLa nuclei with nanobeads, including cells after a NCC-HCC-NCC cycle,
333 were able to pass through mitosis and formed two daughter cells with apparently
334 normal nuclei. Notably, live cell imaging demonstrated mitotic cells with nanobeads
335 excluded from condensed mitotic chromosomes (data not shown, see[40]).

336 In a second set of experiments, we studied movements of microinjected 20 nm
337 sized fluorescent nanobeads in nuclei of live C3H 10T1/2 nuclei, where transient
338 transfection of C3H 10T1/2 cells with a construct for the expression of histone H2B
339 tagged with mRFP[41] allowed the visualization of chromatin[42]. Figure 5f-g shows two
340 nanobeads (green) within such a nucleus at the beginning and the end of a 6h
341 observation period. Figure 5h presents the entire paths travelled by the two
342 nanobeads; Figure 5i indicates that movements occurred most of the time within less
343 dense chromatin (attributed to the ANC), possibly in a random-walk like fashion.

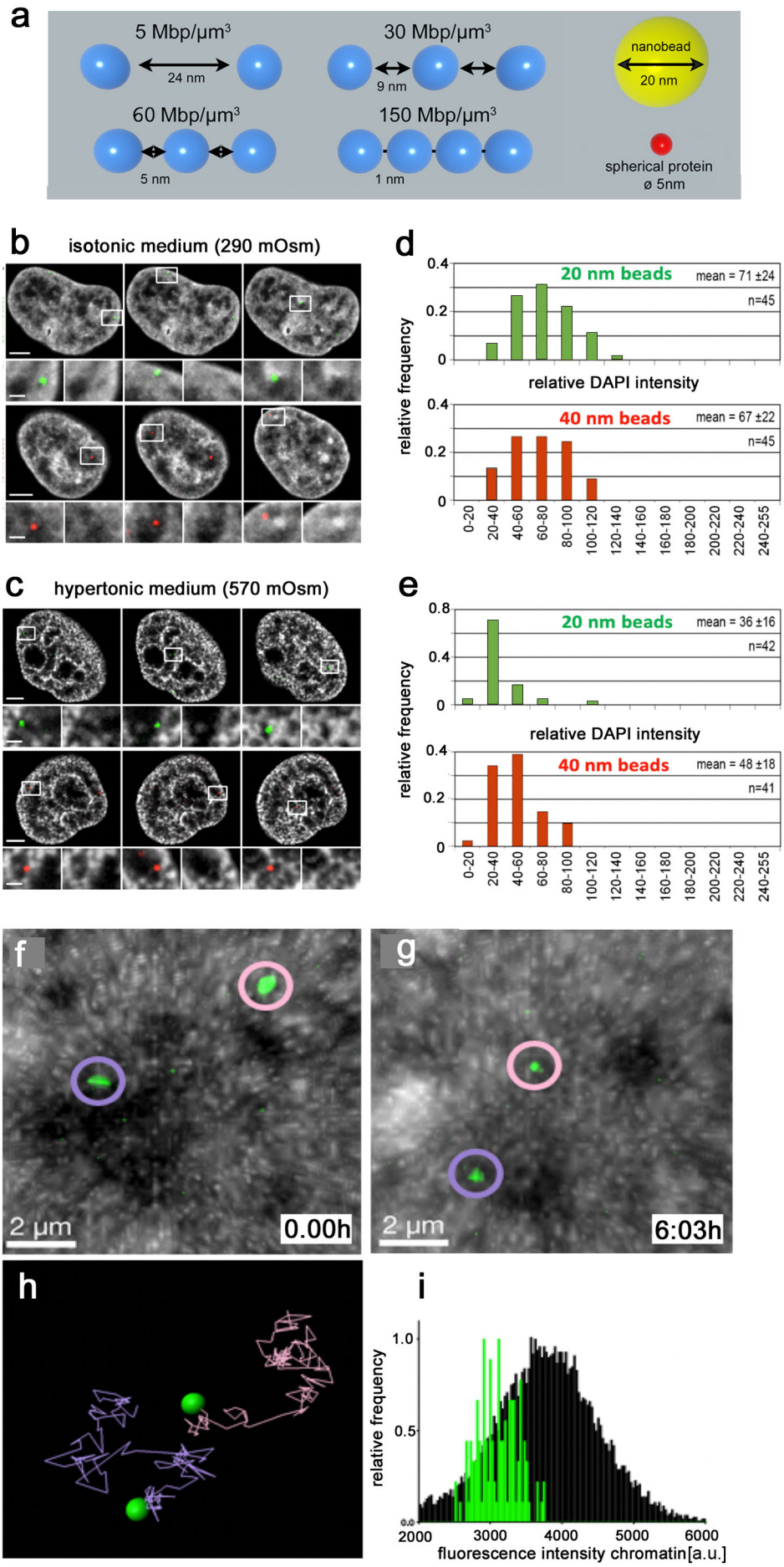
a
5 Mbp/µm³
24 nm
30 Mbp/µm³
9 nm
nanobead
20 nm
60 Mbp/µm³
5 nm
150 Mbp/µm³
1 nm
spherical protein
ø 5nm
b
isotonic medium (290 mOsm)
c
hypertonic medium (570 mOsm)
d
20 nm beads
mean = 71 ±24
n=45
relative DAPI intensity
40 nm beads
mean = 67 ±22
n=45
relative frequency
0-20
20-40
40-60
60-80
80-100
100-120
120-140
140-160
160-180
180-200
200-220
220-240
240-255
e
20 nm beads
mean = 36 ±16
n=42
relative DAPI intensity
40 nm beads
mean = 48 ±18
n=41
f
2 µm
0.00h
g
2 µm
6:03h
h
i
relative frequency
fluorescence intensity chromatin[a.u.]

344

Figure 5: Localization and mobility of microinjected nanobeads within the ANC
a *Distances between surfaces of uniformly arranged nucleosomes (spheres of 10 nm Ø) in 3D space estimated for different DNA densities (5, 30, 60, and 150 Mbp/µm^3), compared to the size of individual macromolecules (Ø 5 nm) and of condensates or macromolecular complexes (Ø 20 nm) (for details see Methods).* ***b-c*** *Live HeLa cells, kept either in isotonic medium (**b**) or hypertonic medium (**c**), were microinjected with 20 nm (green) and 40 nm (red) fluorescent nanobeads and fixed thereafter with PFA. Nuclear DNA was counterstained with DAPI (gray). 3D confocal serial sections were recorded from microinjected cells, and sections with bright nanobead signals (boxed areas) were selected for further evaluation. Magnifications of the boxed areas (lower rows) show nanobeads located within the IC-lacunae (left) together with the DAPI image alone (right) for comparison. Intensity profiles of line scans through individual nanobeads and across the DAPI stained nuclear landscape were analyzed in 40 nuclei (Supplemental Figures S2 and S3). Scale bars: 4 µm in images of whole nuclei, 1 µm in magnifications.* ***d-e*** *Localization of 20 and 40 nm sized nanobeads as a function of relative DAPI intensities in nuclei of cells kept in isotonic (d) or hypertonic medium (e). In both isotonic and hypertonic nuclei, ≥90% of nanobeads are located in regions with DNA densities ≤100 (gray value range 0-256). Mean values are presented with standard deviation. These data demonstrate the location of nanobeads within less dense DNA attributed to the ANC. For further details see[40].* ***f-g*** *In vivo labeling of the chromatin of C3H 10T1/2 cells was performed with a fluorescent protein (mRFP) associated with H2B. Dark and light regions show chromatin of low and high densities, attributed to the ANC and INC, respectively. The two green dots indicate the position of two microinjected nanoparticles at the beginning and the end of the observation period.* ***h*** *shows the whole paths travelled by the two nanobeads.* ***i*** *A comparison of relative mRFP intensities (arbitrary units) across the entire nuclear section (black) with intensities at sites of nanobeads (green) supports the hypothesis that nanobeads move within less dense chromatin, attributed to the ANC (compare Supplemental Video S2).*

Replication of DNA within the ANC followed by relocation into the INC

Two-color experiments illustrate the potential of combining DNA-density maps with the visualization of other markers providing insight into functional states[2,3]. Figure 6a-c shows a two-color image of a HeLa cell nucleus recorded by SMLM demonstrating the topography of replication domains during early S-phase within the ANC. Replication domains (RDs) were observed in particular at the border between the IC and the lining PR, but excluded from dense chromatin of the INC.

In addition, we performed pulse-chase labeling experiments of heterochromatic blocks in undifferentiated mouse embryonic stem cells during mid/late S-phase with EdU (10 min), conjugated with Alexa 488. Serial sections of heterochromatin blocks with structured illumination microscopy (SIM) demonstrated EdU-labeled chromatin

384 within wide IC-channels extending into or throughout their interior (Figure 6d). A chase
385 of 20, 40, 60 and 80 minutes demonstrated the re-location of pulse-labeled chromatin
386 into the neighboring INC, composed of compact heterochromatin lining the IC-
387 channels (Figure 6e-h). This result provides a glimpse into the dynamics of chromatin
388 movements between immediately adjacent ANC and INC compartments (see
389 Discussion).

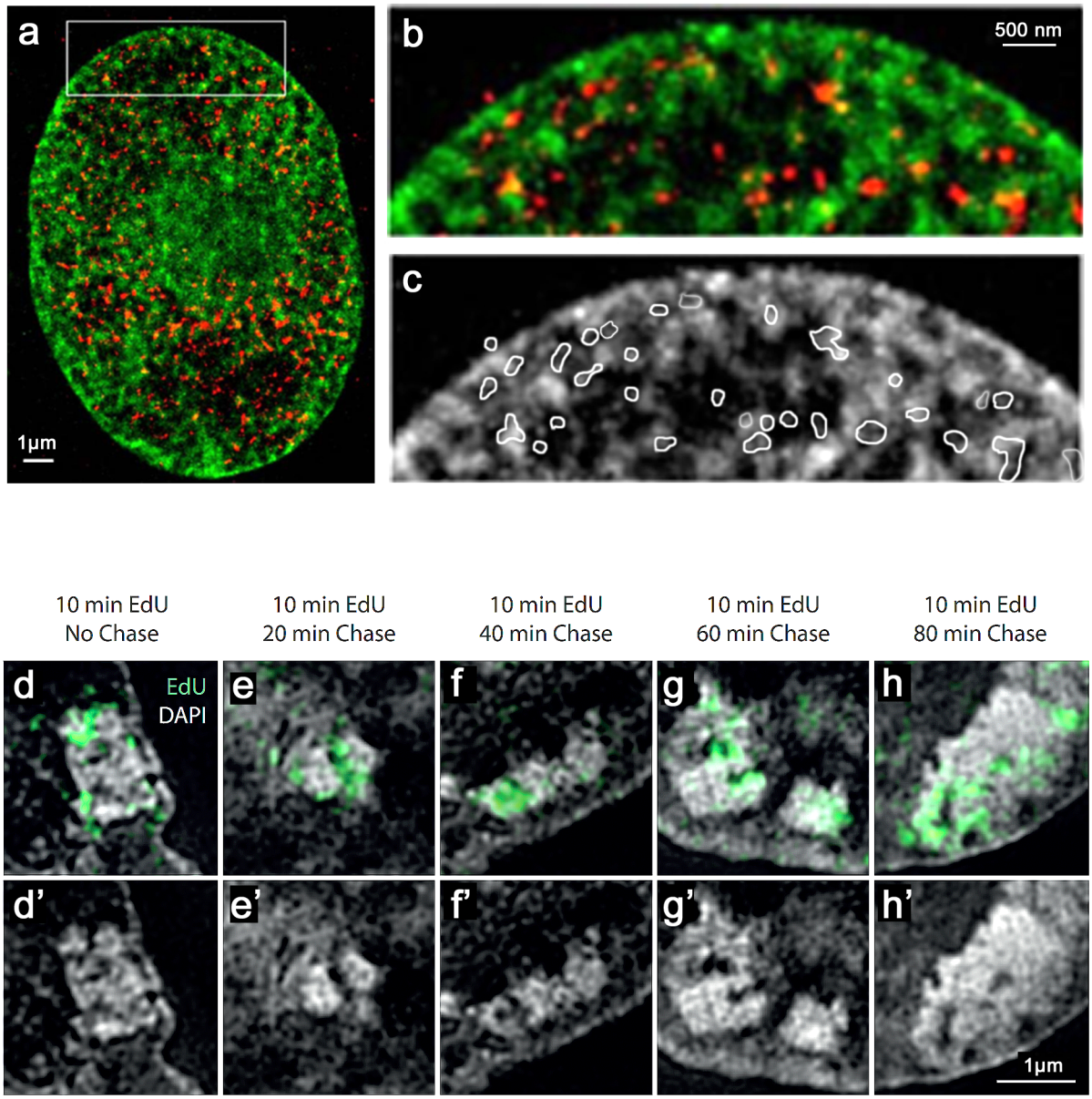

390
391 **Figure 6: Nuclear landscape with replication domains and their relocation from**
392 **co-aligned active to inactive nuclear compartments.**
393 ***a-c*** *Replication domains (red) in a HeLa cell nucleus at early S-phase, recorded with SMLM.*
394 *The cell was fixed immediately after a 15 min pulse-labeling with the thymidine DNA base*
395 *analog EdU, coupled with Alexa Fluor 555. The nuclear section demonstrates the location of*
396 *RDs with newly replicated DNA (red) in the ANC, in particular on the surface of chromatin*

clusters (DNA stained with Vybrant Violet, green). ***a*** *Dual color SMLM image of the entire nuclear section.* ***b-c*** *Magnification of boxed area shown in (a).* ***c*** *White outlines demonstrate the location of most EdU-labeled RDs at the periphery of chromatin domains (white-grey), expanding in section areas (black) attributed to the interchromatin compartment (IC).* ***d-h*** *EdU-pulse-chase experiment of heterochromatic blocks in undifferentiated mouse embryonic stem cells in mid-late S-phase, recorded with SIM. Optical sections show an overlay of DAPI stained DNA (white-gray) and replicated DNA after application of a 10min pulse with EdU (coupled to Alexa488; green).* ***d*** *Cell fixed immediately after the EdU-pulse demonstrates replicated DNA located mostly within low density DNA of wide IC-channels (attributed to the ANC).* ***e-h*** *cells fixed after increasing chase-time of 20/40/60/80 min before fixation show a relocation of labeled DNA into dense DNA of heterochromatic blocks (attributed to the INC).* ***d'-h'*** *DAPI stained DNA only.*

Discussion

In this study, we present examples of nuclear landscapes from human and mouse fibroblasts, a mouse embryonic stem cell, as well as a human cancer cell (HeLa), recorded with entirely different physical principles (SMLM, SIM and ESI). With SMLM-fBALM, the positions of millions of 'blinking' DNA-bound reporter fluorophore positions (SMPs) in optical nuclear sections were obtained with an average lateral resolution of ~20 nm within the object plane and an axial resolution of ~100 nm. Accordingly, the estimated observation volume[43] was about 500x smaller compared to conventional wide-field fluorescence microscopy. Hence, the 3D structural resolution was enhanced by this factor. High-resolution DNA density maps generated from SMLM-fBALM images revealed absolute DNA compaction differences in nuclei of fixed cell samples from <5 Mbp/µm^3 to >300 Mbp/µm^3, a range much higher than previously published (see Introduction). The high structural resolution of DNA-density landscapes achieved with SMLM-fBALM required the spatial mapping of millions of SMPs in single light optical nuclear sections. This was achieved with the consecutive recording of many thousand individual image frames with ~50 ms for each frame. Hence, the stability of the SMLM setup is of utmost importance to avoid drifts during very long total recording times (up to 40 min in the present study or even longer). Our custom setup was built to meet this requirement.

429 Monte-Carlo simulations[16] have predicted accessibility constraints for
430 nucleosomal concentrations in the order of 0.3 mM to 0.5 mM (reflecting 40 –
431 60 Mbp/μm^3 in case of DNA fully compacted with nucleosomes). Based on these
432 simulations and our new results, we provisionally attribute chromatin with less dense
433 DNA (<40 Mbp/μm^3) to the active nuclear compartment (ANC), and chromatin with
434 denser DNA (>40 Mbp/μm^3) to the inactive nuclear compartment (INC). To explore
435 mechanical accessibility barriers imposed by densely packaged chromatin attributed
436 to the inactive chromatin compartment (INC), we microinjected fluorescent beads with
437 diameters of 20 nm and 40 nm, reflecting sizes typical for transcription- and replication-
438 complexes, into nuclei of living cells. We observed that these nanobeads were
439 excluded from the INC, but able to move within the less dense chromatin of the ANC.
440 These results are consistent with previous live cell fluorescence microscopy of artificial
441 nuclear bodies built up from clustered plasmids with inducible transgenes[44]. Artificial
442 bodies were formed within the IC and stayed there during interphase independent of
443 their silent or induced active state, suggesting that their size prevented diffusion into
444 the lining chromatin. Activation of transgene transcription resulted in the recruitment of
445 RNA polymerase II and NFκB and a closer positioning to splicing speckles. Upon entry
446 of cells into mitosis, the bodies were never trapped within, but always separated from
447 mitotic chromosomes.

448 The following discussion highlights major functional implications of our new
449 findings, as well as present methodological limitations, which need to be overcome for
450 compelling further experimental tests. Our new observations together with published
451 results support the hypothesis that functional machineries are size-excluded from the
452 compact interior of chromatin ensembles with DNA densities allocated to the INC[2,16].
453 Notably, conformational changes may allow that all spaces within a chromatin hydrogel
454 can be accessed at some time. The probability, however, that a transcription factor, for

455 example, successfully binds within dense chromatin regions is statistically much less
456 likely compared to lesser compacted regions. The examples of nuclei shown in this
457 study for a human fibroblast (BJ1) a human cancer cell (HeLa) and a mouse fibroblast
458 (C3H T1/2) support typical architectural features of the ANC-INC model, arguably
459 because these features are indispensable for functional reasons in both diploid and
460 aneuploid cell nuclei. Many nucleosome clusters have sizes in the order of about
461 100 nm or even less and therefore their spatial conformation cannot be further
462 analyzed by microscopy at conventional resolution. In line with our present study, a
463 series of previous microscopic studies with SMLM[45], and structured illumination
464 microscopy (SIM)[3,10,46] has provided evidence for major functional roles of chromatin
465 ensembles located in the ANC, including transcription and DNA replication[47]. In
466 addition to functionally active chromatin ensembles located in the perichromatin region
467 (PR)[48], chromatin/DNA loops apparently extrude from the PR into the interchromatin
468 compartment (IC). Arguably, large and highly expressed genes in normal cell types[49],
469 as well as highly expressed amplicons of genes in cancer cells[50], expand along IC-
470 channels through the nuclear space into and even through neighboring CTs. These
471 observations, however, do not contradict the hypothesis that loops formed by most
472 active genes are small-sized. A schematic model of a chromatin domain (Figure 7a
473 adapted from[46]) argues for small loops with active histone marks (green dots),
474 associated transcription factors and RNA polymerase complexes located at the CD
475 periphery (ANC). In contrast, nucleosomes with repressive histone marks locate within
476 the repressed CD core (INC), where they are inaccessible for the transcriptional
477 machinery. This model implies that transcriptional repression or activation may depend
478 on mechanisms for the 3D re-location and epigenetic remodeling of nucleosomes with
479 important target sequences, such as from the transcriptionally competent CD periphery
480 into the silent interior and vice versa from the interior to the periphery for activation.

481 Notably, such a re-location mechanism allows stochastic heterogeneity of the positions
482 of nucleosomes whose exact positions may be functionally irrelevant, but requires a
483 functionally indispensable preciseness of the space-time organization of CDs only for
484 those nucleosomes which carry important DNA target sequences, such as
485 transcription regulatory elements (Figure 7b)[51]. For example, we consider regulatory
486 and coding sequences of active genes required within the ANC in cycling cells. Their
487 relocation into the compact chromatin of the INC in postmitotic, terminally differentiated
488 cells would provide a structural mechanism to safeguard long-term silencing. In case
489 that regulatory sequences of such genes become inaccessible in the interior of highly
490 compact domains, their accessibility would require chromatin decondensation to an
491 extent that allows constrained movements of required transcription factors into the
492 domain interior. Similar structural mechanisms may be envisaged for movements of
493 DNA between neighboring parts of the ANC and INC required for DNA replication (this
494 study), as well as potential movements involved in DNA repair[48,52]. In line with the
495 hypothesis that DNA repair is performed within the ANC, particularly large-sized,
496 radiation-induced γ-H2AX repair foci with diameters of up to 1 µm were described,
497 composed of partially elongated subfoci with an overall size of ≤100 nm[53]. Still, it is not
498 clear, how chromatin nanostructures form higher levels of chromatin organization.
499 Employing electron tomography, Zakirov et al. [54] demonstrated a fiber-like higher-order
500 structure of about 200 nm in diameter (chromonema) of EdU-labeled chromatin (2 h)
501 detected with biotin-streptavidin-mediated nanogold.

502 The nuclear matrix proteome[55] may form phase-separated droplets within the
503 IC with the help of non-coding RNA sequences[56,57]. Like assembled macromolecular
504 machineries, such condensates are excluded by size from the INC and may serve as

storage vesicles for the formation of functional machineries. For example, Scaffold Attachment Factor A (SAF-A), was observed in the ANC[47], and our unpublished data.

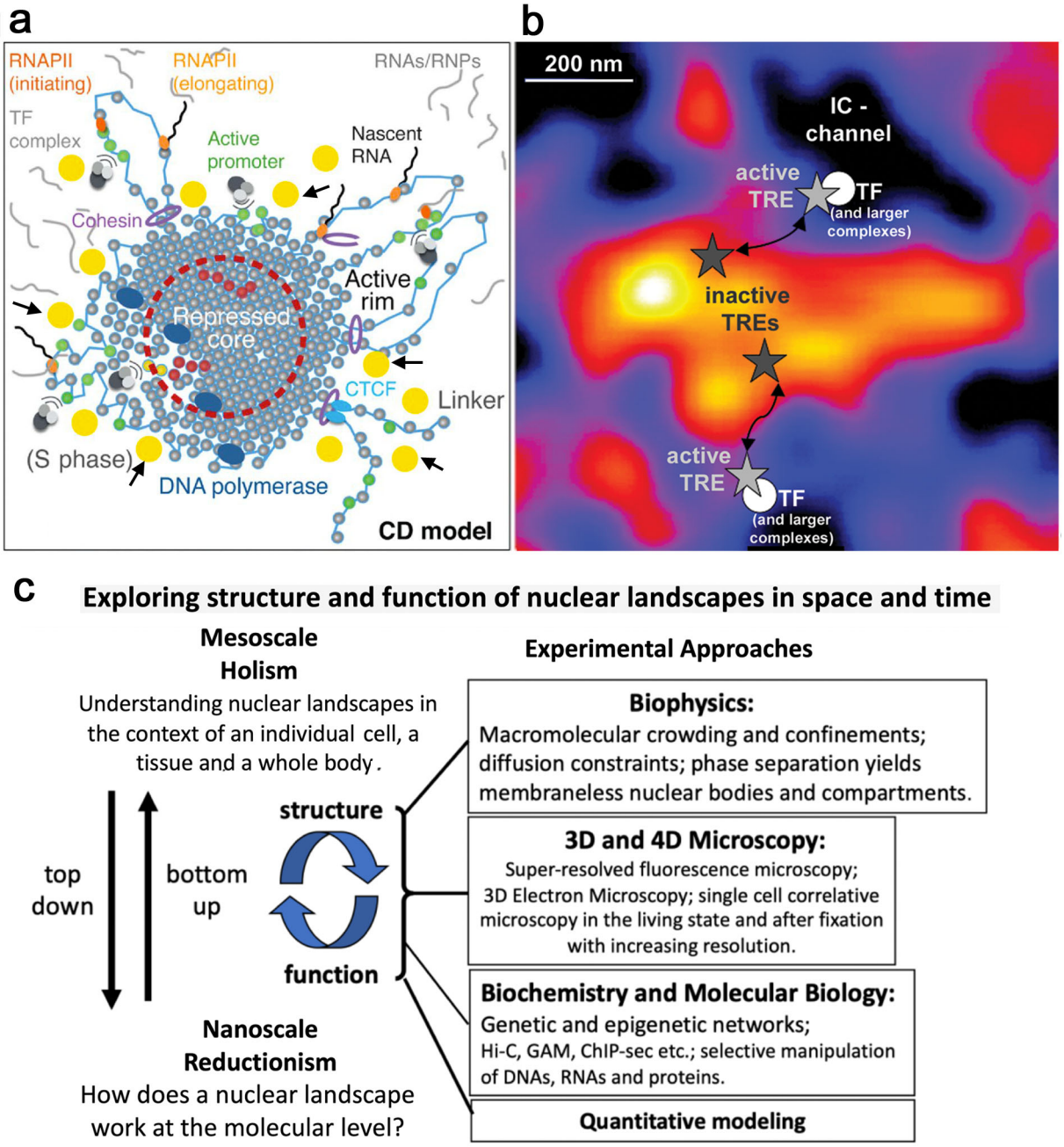

Figure 7: Nanoscale and mesoscale topography of the nuclear landscape

a *Nanoscale model of a chromatin domain adapted from[46]. It presents a chromatin domain with a repressed core of densely compacted nucleosomes and an active rim with expanding, transcribed chromatin loops. Yellow dots (some of them marked by small arrows) are added to indicate phase-separated, 20-nm sized droplets.* ***b*** *Mesoscale model of functionally interacting active and inactive nuclear compartments[51]. The ANC-INC model proposes functional interactions between the ANC and INC based on hypothetical bidirectional chromatin movements, such as genes and corresponding transcription regulatory elements (TREs), from the ANC into the INC for long-term silencing, and from the INC to the ANC in case of renewed transcriptional activation. In this hypothetical nuclear section, the INC is represented by a chromatin domain cluster with several high-density peaks (white-yellow) and surrounding slopes (red), embedded within the ANC with its much less compacted chromatin.*

520 *The ANC is composed of transversely cut IC-channels (black) and the lining perichromatin*
521 *region (PR) (blue). Dark stars indicate the location of inactive TREs within the INC, light grey*
522 *stars the position of active TREs in the ANC.* ***c*** *An integrative experimental approach to explore*
523 *the intricate space-time, structure-function-conundrums of nuclear landscapes at nanoscale*
524 *and mesoscale.*
525
526 Molecular mechanisms guiding structure-function relationships at nanoscale
527 and mesoscale are still not well understood. For an in-depth understanding of these
528 relationships, it is mandatory to integrate microscopic methods with other biophysical
529 and biochemical approaches (Figure 7c). Cryo-electron microscopy has great
530 advantages with respect to the preservation of nanoscale structures[58], but it is difficult
531 to keep these advantages in attempts to combine cryo-EM with immuno-EM and FISH
532 protocols. Detailed comparisons of the best resolved microscopic maps with maps
533 based on Hi-C, ChIA-Pet and GAM[59,60], as well as molecular chromatin accessibility
534 profiling methods[61] will help to produce fully integrated, high-resolution maps, which
535 overcome current deficits.
536 Recent evidence has suggested a dual nature of chromatin[62,63]. Transitions
537 between liquid and solid states of chromatin ensembles are still not well understood[62].
538 Whereas constrained local motions of nucleosomes occur on the seconds timescale,
539 solid chromatin at mesoscale does not mix with its environment on the minutes to hours
540 timescale. Phase-separation has been implicated in euchromatin and heterochromatin
541 formation in a complex interplay with epigenetic mechanisms[64]. Chromosome
542 territories apparently form a polymer network with material properties of an elastic
543 hydrogel[62]. While a liquid state of 200 nm sized chromatin domains would enable the
544 efficient activation of genes through diffusion-mediated, long-range regulatory
545 contacts, the possibility that 200 nm domains exist as a solid gel state and exert gel-
546 like sieving effects may also be considered. Evidence for a gel-like chromatin
547 organization at mesoscale suggests a porous structure of the chromatin landscape
548 with sieving effects affected by global or linear shapes of diffusing macromolecules[65-

549 [67]. Phase-separated droplets, carrying an assembly of macromolecules (proteins, non-
550 coding RNAs) required for specific nuclear functions, may interact with chromatin
551 domains with gel-like properties. Such complex interactions are not explained by
552 models of an exclusively size-dependent accessibility. For example, the penetration of
553 small macromolecules assembled within such droplets into the interior of dense
554 chromatin may be prevented, whereas percolation of individual, larger
555 macromolecules is still possible.

556 A recent polymeric model of higher order chromatin arrangements at mesoscale
557 was based on phase separation of chromatin, considering two key features, namely
558 chromatin self-attraction and its binding to the peripheral lamina[68,69]. It offers a
559 biophysical mechanism for the overall determination of nuclear chromatin density and
560 hence accessibility by the regulation of lamina-chromatin interaction strength. Such a
561 quantitative numerical model may help in part to explain physical properties of the
562 ANC-INC model[2,10,70]. Other polymeric models provide similar interaction principles to
563 control the density and hence accessibility of individual gene domains[71]. Computer
564 models of chromatin nanostructures performed under various biochemical
565 assumptions, such as histone linker length, Mg^{2+} concentration, acetylation, histone
566 interactions, or epigenetic marks argue for highly complex nanostructures containing
567 relatively open parts as well as small regions with an apparent chromatin density
568 sufficiently high to constrain the access of individual macromolecules, likely preventing
569 the penetration of larger aggregates[18,72-74]. Bascom et al.[75] performed numerical
570 simulations based on Hi-C and epigenetic data of the 55 kbp-sized HOXC gene for a
571 series of 3D configurations representing inactive and active chromatin states, compare
572 Figure S3 in[75]. Extended model configurations show highly condensed clusters of
573 densely packed nucleosomes connected by stretches of nucleosome-free DNA, i.e.,
574 highly accessible sites. From the volumes within the enveloping surfaces of these

575 ensembles, one can estimate average densities ranging from ~7 Mbp/μm^3 to ~20
576 Mbp/μm^3. These average estimates, however, do not allow conclusions about the
577 actual densities of structures below the resolution limit. Direct imaging of such
578 structures remains an unsolved challenge and would likely require a 3D structural
579 resolution of a few nm. Furthermore, the Voronoi tessellation approach used in our
580 present study is particularly useful to measure local DNA densities, likely
581 corresponding to small nucleosome clusters, but fails to detect loops formed by
582 extended stretches of naked DNA or ~10 nm thick nucleosomal chains.

583 Constrained spatial accessibility due to dense chromatin compaction of the INC
584 is not the only barrier preventing/attenuating the diffusion of proteins and RNAs from
585 the nucleosome free space of the ANC into the INC[25]. Other features, such as electric
586 charge[76] and the enrichment of macromolecules within phase-separated droplets, may
587 also affect the accessibility of chromatin ensembles. In addition, for more sophisticated
588 models of chromatin accessibility, it would be important to achieve more information
589 about the space-time distribution and structure of genomic regions with a depletion or
590 even complete loss of nucleosomes[77,78]. To which extent, dense convolutes of naked
591 DNA may exist in the ANC has remained elusive.

592 Finally, we wish to emphasize major limitations of our present DNA-density
593 maps of nuclear landscapes. The high structural resolution achieved with SMLM
594 required fixed cells. We employed protocols that maintain 3D nuclear shape and
595 topography of CTs, nuclear speckles, replication domains and 3D positions of genes
596 to a remarkable extent down to the lateral and axial resolution limit of 3D-SIM (x,y ~
597 100 nm and z ~ 250nm)[79,80]. It is essential to keep living cells in their normal osmotic
598 environment[39] and avoid drying out of preparations during fixation and all subsequent
599 steps until embedding for microscopic examination. A potential impact of fixation
600 artifacts on large-scale chromatin organization was previously tested in 3D-SIM live-

601 cell experiments with HeLa cells stably expressing histone H2B-GFP (see additional
602 file 8 in[47]). Live and fixed cells showed a high degree of similarity with regard to
603 chromatin clusters, sites of decondensed chromatin, IC lacunae and IC channels
604 leading to nuclear pores. We cannot exclude, however, fixation artifacts of active and
605 inactive chromatin ensembles at nanoscale below the resolution limit of 3D-SIM.

606 True-to-scale DNA density maps should be complemented by similar density
607 maps based on nucleosome positions as an essential basis for modeling of chromatin
608 accessibility. Ideally, one would like to follow the dynamics of any target sequence of
609 interest within a given chromatin ensemble and explore in living cells the dynamic
610 compaction of individual loops or nanodomains comprising a few kb and the potential
611 opening and closing of IC-channels. The generation of such space-time nuclear maps
612 requires the development of time-resolved super-resolution microscopy approaches of
613 live cells[20,81-84]. The space-time visualization of chromatin ensembles is essential for
614 studies to solve the question of intermingling loops between neighboring CTs[48,85].
615 Furthermore, an appropriate toolset should allow the integration of epigenetic marks,
616 RNAs and non-histone proteins into individual chromatin ensembles across the entire
617 nuclear landscape[86,87]. Steadily improved, color-coded, high-resolution maps of
618 nuclear landscapes are ideally suited to incorporate huge datasets of additional genetic
619 and epigenetic information in an intelligible manner, providing direct insight into the
620 interdependence of structural and functional changes[88-90]. This is a long way to go not
621 only with regard to the challenges of developing high resolution 4D live cell microscopy
622 but also in view of the requirements of comprehensive, high-throughput 4D image
623 analyses of large cell numbers. The reward will be worth all the effort. Changes of
624 nuclear landscapes during differentiation and development of numerous cell types
625 provide an important enrichment to the Human Biomolecular Atlas Program[91].
626 Evolutionary comparisons will shed new light on the origin of cell nuclei[92] and the

627 evolution of metazoan chromosomes[93]. Based on the emerging evidence that physical
628 compaction and decompaction of chromatin nanodomains play a major role in gene
629 regulation not only in eukaryotes but also in prokaryotes[94], it is interesting to explore
630 to which extent differences between high-resolution DNA density maps of different cell
631 types[90] correlate with and may predict global transcriptional differences.
632

633 **Acknowledgments**

634 Márton Gelléri, Shih-Ya Chen, Aleksander Szczurek, Jan Neumann, and Christoph
635 Cremer were supported by the Boehringer Ingelheim Foundation and the Max Planck
636 Institute for Chemistry, Mainz (Germany). Hilmar Strickfaden and Michael J. Hendzel
637 were supported by grants from the Canadian Cancer Research Society (grant number
638 CRISDI 2018 OG 23446) and the Canadian Institutes of Health Research (grant
639 number PJT-148753). We are obliged to many colleagues for helpful suggestions. In
640 particular, we thank in alphabetical order Udo Birk, Giacomo Cavalli, Jonas Cremer,
641 Mario Nicodemi, Thoru Pederson, Katharina Ribbeck, Karsten Rippe, Vassilis Roukos,
642 Samuel Safran, and Nadine Vastenhouw for critical reading and discussion. We thank
643 Sandra Ritz and all the members of the IMB Microscopy Core Facility for technical
644 support.
645

646 **Author contributions**

647 CC, HS, MG, MC and TC planned this study and wrote the manuscript. All authors
648 contributed to the final text. S-Y C and CC developed the SMLM instrumentation; AS
649 developed the fBALM approach and contributed experimental SMLM results. SMLM-
650 images of nuclear landscapes were recorded by S-Y C, MG, HS, and AS, electron
651 spectroscopic images by HS. Quantitative Voronoi-analyses of SMLM sections were
652 carried out by MG, analysis of ESI images by HS and MH. Evaluation algorithms were

653 provided by MG, JN, OK, FS, HS and JI. These authors also contributed to the various
654 approaches of SMLM image displays and analyses. Microinjection experiments with
655 fluorescent nanobeads and quantitative analyses were conducted by BH and HS. EdU-
656 replication-labeling experiments with SMLM were performed by AS. MS carried out 3D
657 SIM studies of EdU-pulse-chase experiments with guidance from YM.
658

659 ## Material & Methods

660 **Cell cultures, fixation, and staining protocols**

661 h-TERT BJ1 cells, immortalized, diploid human cell line from human foreskin
662 fibroblasts (ATCC #CRL-2522), HeLa cells, a human cervix carcinoma derived cell line
663 with a near-triploid karyotype (n = 68-70[95]), and C3H 10T1/2 cells, derived from murine
664 embryo fibroblast cell line (ATCC #CCL-226)[96] were cultured in DMEM with 5% CO_2
665 at 37 °C. Undifferentiated female mouse embryonic stem cells (ESC line 16.7, 42,XX;
666 +6;+8, kindly provided by J. Lee, Harvard Medical School) were cultivated under
667 feeder-free conditions on gelatinized cover slips in KO-DMEM (Invitrogen) as
668 described in details elsewhere[47]. After fixation with formaldehyde (4%) for 15-30 min,
669 cells were kept in Dulbecco's Phosphate Buffered Saline (DPBS, Sigma Aldrich) and
670 incubated with 0.5 U/ml RNase A and 20 U/ml RNase T1 (Ambion, USA) for 1 h at
671 37 °C. Care was taken to avoid any air drying of cells throughout the entire procedure
672 in order to maintain the shape, volume and internal structure of cells as best as
673 possible[79,80]. Nuclear DNA was stained with DAPI, or with Sytox Orange (Thermo
674 Fisher) for super-resolution microscopy (SMLM) in the fBALM (fluctuation assisted
675 Binding Associated Localization Microscopy) mode (see below), as described[35,36].
676 With a size in the 1 nm range, the accessibility of Sytox Orange and Vybrant Violet
677 should not be substantially impaired by chromatin compaction per se.
678

679 **Determination of cell cycle & nuclear morphology**

680 Determination of cell cycle stage and nuclear morphology of BJ1 and HeLa cells was
681 performed using a spinning disk Opera Phenix Plus High-Content Screening System
682 (PerkinElmer), according to[97], with Sytox Orange as a DNA stain. For SMLM-fBALM
683 measurements, nuclei were used with sizes equal or below the average G1 value for
684 each cell type. Imaging was performed in wide field mode with a 20x, 0.4 NA objective
685 to capture fluorescence from interphase cells and mitotic cells without the need of
686 recording a z-stack. In each well, multiple images were acquired, covering
687 approximately 80 percent of a single well resulting in 20,000 to 80,000 imaged cells
688 per well. Nuclear area and fluorescence intensity of Sytox Orange was analyzed by
689 segmentation with Harmony software (PerkinElmer). Nuclei that were touching the
690 image border were excluded from further analysis. The frequency distribution of Sytox
691 Orange intensities showed discrete G1 and G2 cell cycle populations that allowed the
692 classification of each cell nucleus into these classes.

693

694 **Microinjection of fluorescent nanobeads (FluoSpheres)**

695 Microinjection of carboxylate-modified FluoSpheres (Thermo Fisher) with a diameter
696 of 20 nm and 40 nm into nuclei was performed on an Axiovert 200 M widefield
697 microscope (Zeiss) with an injection system from Eppendorf. Needles were pulled from
698 borosilicate glass capillaries with an outer diameter of 1.0 mm and an inner diameter
699 of 0.5 mm using a micropipette puller (Sutter Instrument P-97; for details see[40]).

700

701 **Pulse-labeling of replication domains (RDs) with EdU**

702

703 For SMLM experiments, RDs were identified following pulse-labeling of HeLa cells for
704 15 min with 5-Ethynyl-dU (EdU) at a final concentration of 10 µM as described[10,45].
705 EdU was conjugated to AlexaFluor 555 by click-chemistry according to manufactures

706 instructions (https://www.thermofisher.com/). Cells were washed in PBS, fixed with 4%
707 formaldehyde/PBS for 15-30 min and permeabilized with 0.5% Triton X-100/PBS/
708 Tween 0.02% for 10 min. DNA was counterstained with Vybrant Violet, a fluorescence
709 dye with a predominant affinity for DNA[98]. For 3D-SIM experiments, RDs in mouse
710 embryonic stem cells were identified by an EdU pulse of 10 min. Cells were fixed
711 immediately with 2% formaldehyde, or after a chase of 20 - 80 minutes. DNA was
712 counterstained with DAPI (1 mg/ml). Cells were postfixed in 4% formaldehyde and
713 mounted in antifade mounting medium (Vectashield Vector Laboratories).
714

715 **Distances between surfaces of uniformly arranged nucleosomes in 3D space**
716 **estimated for different DNA densities**

717 We assumed that the entire genome was fully packaged with nucleosomes, i.e. that
718 each consecutive 200 bp DNA segment carried a nucleosome with ~150 bp of DNA,
719 wrapped around the core histone complex, and a linker length of ~50 bp between any
720 two linearly adjacent nucleosomes located on the same ~10 nm nucleosomal chain. In
721 case of fully extended linker DNA, this means a maximum distance of ~15 nm. Next,
722 we determined the maximum number and spatial distribution of nucleosomes that can
723 be placed at a given DNA density into a 1 μm^3 cube under the highly simplified
724 assumption of homogenously distributed, equidistant nucleosomes. Placing each
725 nucleosome (represented by spheres with 10 nm diameter) with its center into a sub-
726 cube, we calculated the center-to-center 3D distances between adjacent nucleosomes
727 placed in the midst of these sub-cubes; from this, the minimum average 3D distances
728 between the surfaces of spatially adjacent spherical nucleosomes were determined for
729 average DNA densities of 5, 30, 60 and 150 Mbp/μm^3. For example, a cube of 1 μm^3
730 with an average DNA density of 150 Mbp/μm^3 contains ~750,000 nucleosomes placed
731 at a mean 3D distance of ~1 nm between the surfaces of any two nucleosome

732 neighbors adjacent in 3D space. In contrast, a 1 μm^3 cube with an average DNA
733 density of 5 Mbp/μm^3 contains only ~25,000 nucleosomes with a minimum 3D distance
734 of ~24 nm. Note that many next nucleosome neighbors in 3D space may be located at
735 different DNA sites of the same nucleosomal chain or on different spatially adjacent
736 loops. This explains why the minimum average distance calculated for 5 Mbp/μm^3
737 exceeds the maximum length of ~15 nm for a fully stretched 50 bp DNA linker.

738 These estimates cannot replace sophisticated modeling, taking into
739 consideration the constraints of polymer chain folding of 10 nm thick nucleosomal
740 chains[99]. Notably, highly compacted chromatin does not provide much freedom for
741 local changes of accessibility resulting from a dynamic, non-uniform distribution of
742 nucleosomes. Whereas the accessibility of the interior of a loop forming a dense
743 nucleosome cluster is highly constrained[16], such constraints may barely matter in case
744 of an open loop configuration (compare Figure 1c).

745

746 **Single Molecule Localization Microscopy (SMLM)**

747 For studies of high-resolution DNA density maps with SMLM-fBALM (fluctuation-
748 assisted Binding Activated localization microscopy) mode[35,36] an inverse custom-made
749 localization microscope was equipped with three lasers emitting at 488 nm, 561 nm
750 and 647 nm. The three lasers were combined with dichromatic reflectors. The laser
751 beams were expanded by a pair of lenses and focused to the back focal plane of the
752 objective lens (HCX PL APO 100x/NA 1.47 oil, Leica, Germany) by a tube lens. A
753 quadband dichroic mirror was used to reflect the laser and to transmit emitted
754 fluorescence light from the sample. In this setup, a Gaussian intensity distribution with
755 a full width at half maximum (FWHM) of 50 µm was created in the focal plane of the
756 objective lens.

757 fBALM relies on the spatial switching of fluorescent on/off states by adjusting
758 the local environment of the DNA and DNA-binding sites. The chemical environment,
759 in particular the pH value, allows control over the local, reversible DNA melting of
760 double stranded into single stranded DNA. Sytox Orange binds to dsDNA, falls off after
761 local melting from ssDNA, and rebinds to dsDNA, usually at another site. Unbound
762 Sytox Orange molecules have a fluorescence up to several orders of magnitude lower
763 than the emission of blinking DNA-bound molecules. Furthermore, unbound Sytox
764 Orange molecules have a much larger mobility. Hence their weak fluorescence
765 emission forms a rather homogeneous background which can be removed by
766 appropriate image analysis tools[100]. In summary, fBALM provides both a substantial
767 reduction of background combined with a very high number of blinking events of
768 dsDNA bound fluorophores, which is only limited as a consequence of either complete
769 bleaching of the entire pool of Sytox Orange molecules, a change of the chemical
770 environment, or of an optical instability of the SMLM setup.

771 SMLM-fBALM allowed the determination of single-molecule positions (SMPs) of
772 Sytox Orange molecules in nuclei with a typical average precision of σ_{xy} ~8 - 15 nm
773 (object plane; best values around 2 nm in heterochromatic regions), and an axial
774 precision σ_z down to about 50 nm. From these figures, an average lateral optical
775 resolution OR_{xy} (smallest lateral distance detectable between two molecule positions)
776 of 20 nm was obtained for σ_{xy} = 8.5 nm, and around 100 nm for OR_z along the optical
777 axis. For molecule positions with a localization precision (object plane, xy) of 2 nm, the
778 best OR_{xy} value estimated was around 5 nm. Experimentally, in nuclear sections of
779 HeLa nuclei, selected single molecule positions with σ_{xy} ≤5 nm and mutual xy-
780 distances of 11 nm and of 14 nm, respectively, were clearly distinguished. For the
781 object plane coordinates with σ_{xy} = 8.5 nm and d (SMPs/nuclear area = 10^7/100 μm^2 =
782 0.1/nm^2), the average structural resolution R (as a measure for the smallest observable

783 structure) was estimated according to $R = [(2.35\ \sigma_{xy})^2 + (4/d)]^{0.5}$ [34]. From this, R =
784 21 nm was obtained if all 10 million molecule positions localized are included in a 600
785 nm optical section. For a thinner optical section of about 100 nm with 1.5×10^6 molecule
786 positions, R = 26 nm was estimated. If in addition the average drift (after correction) is
787 included[98], then the average R increases from 21 nm to 23 nm, and from 26 nm to
788 28 nm, respectively.

789 Selected HeLa and BJ1 cells were placed in the center of the field of view of the
790 inverted SMLM-microscope. Nuclei were exposed to the 561 nm laser at an estimated
791 illumination intensity of about 1 kW/cm^2. Fluorescence was collected by the objective
792 lens and was separated from the excitation laser by a dichromatic beam splitter and
793 appropriate emission filters. The emission light was focused by a second tube lens and
794 imaged on an sCMOS camera (PCO edge 4.2) with a pixel size corresponding to
795 65 nm in the object plane, setting the exposure time to 50 ms/frame. Up to 50,000
796 frames with a total of ~10 million blinking events were recorded in single ~600 nm thick
797 light optical section and localized with appropriate localization algorithms[34,100]. The
798 possibility that the same fluorophore was recorded twice (double blinking event) was
799 considered in cases where two signals recorded in subsequent image frames had a
800 distance smaller than 20 nm. These rare events were excluded from further image
801 analysis as described below. To localize SMPs from a thinner section than 600 nm,
802 achieved with conventional wide-field resolution, a cylindrical lens was placed in front
803 of the sCMOS camera[101] to induce an astigmatism[102]. In this way it was possible to
804 assign SMPs to positions ± 50 nm above or below the focal plane and thus filter out
805 the SMPs in a ca. 100 nm thick optical section (assumed to be ca. 1/6th of the total
806 number of SMPs in the 600 nm optical section).

807 For recording of DNA densities and replication domains (RDs) with dual-color
808 SMLM[98], a custom-built, upright-setup [103] was used, equipped with lasers for excitation

809 wavelengths 405 nm and 491 nm, respectively [98]. EdU-labeled RDs were conjugated
810 to AlexaFluor 555 and recorded first (5,000 SMLM frames). Vybrants DyeCycle™
811 Violet (VdcV) was used to label the non-replicated DNA[98]. After photoconversion with
812 405 nm, Vybrant Violet was excited to 'blink' by intense 491 nm illumination, and the
813 emitted green fluorescence was registered (30,000 frames).
814

815 **Estimation of true-to-scale DNA density values**

816 The procedure we have used to achieve true-to-scale DNA density values is illustrated
817 in Supplemental Figure S1 using the BJ1 light optical section presented in Figure 2.
818 The reliability of 3D DNA density values for a given chromatin ensemble critically
819 depends on the determination of both its absolute DNA content and its volume. Several
820 essential requirements for precise measurements of these values need to be
821 considered.

822 First, our concept assumes that fluorophores like YoYo[45] or Sytox Orange[35] bind
823 randomly, i.e. without base-pair preference, to the nuclear dsDNA, and can be
824 localized with high precision by SMLM. The lateral nuclear positions of SMPs (within
825 the object plane) were determined with an average precision of 8 - 15 nm. This requires
826 extreme mechanical stability of the microscopic setup[104,105]. The determination of the
827 axial positions of SMPs[101] was not further defined, but assumed to reflect the thickness
828 of the light optical section, which was about 600 nm in the example HeLa cell nucleus
829 (Figure 3). In the case of the BJ1 nucleus (Figure 2), the use of an astigmatic lens[102]
830 resulted in an improved axial localization precision of SMPs down to about 50 nm in a
831 100 nm thick optical section. Under optimal conditions, lateral nuclear SMP distance
832 differences <5 nm were detected. The pixel size for the density determination was
833 adapted to reflect the mean localization precision of the SMLM measurements. For

834 volume estimates of light optical sections, we assumed a thickness of 100 nm in SMLM
835 setups with an achromatic lens and of 600 nm without such a lens.

836 Second, for estimates of the total DNA content of an entire nucleus or a given
837 light optical section, it is necessary to determine the interphase stage of the studied
838 cell. Cell cycle measurements (see above) indicated that the cells subjected to fBALM
839 were in G1. In the case of cells with an abnormal chromosome content, such as HeLa
840 cancer cells, it is preferable to measure the DNA content of a single, studied cell
841 nucleus (not performed here) or to provide an estimate based on knowledge of the
842 karyotype, though this karyotype may differ from cell to cell. For BJ1 cells we assumed
843 a diploid karyotype (2n), and for HeLa cells a near triploid karyotype (3n).

844 Third, the calibration of absolute DNA density values should ideally be based
845 on the total number of SMPs, recorded from an entire cell nucleus in a stack of optical
846 serial sections. This total number then reflects the total DNA content, whereas the
847 number of SMPs recorded within a single section provides the fraction of genomic DNA
848 present in this section. In practice, the decrease of blinking efficiency due to a
849 deterioration of the chemical switching conditions[36] during the long registration times
850 makes it presently difficult or impossible to obtain serial SMLM sections of entire nuclei
851 with high structural resolution. For this reason, we typically performed a single SMLM
852 midsection from nuclei with high 3D structural resolution (i.e. a high average SMP
853 density) and assumed a linear relationship between volume and DNA content,
854 neglecting the evidence for highly non-uniform distribution of DNA within active and
855 inactive nuclear compartments, (see[45,47]). Preliminary experiments based on SMLM
856 serial sections of HeLa cell nuclei at lower structural resolution (data not shown) argue
857 that this simplifying assumption yields reasonable DNA estimates. Furthermore, for
858 chromatin regions with a size equal or larger than the conventional resolution limit,

859 these estimates are similar to those obtained in absolute calibration studies using
860 Fluorescence Correlation Spectroscopy and confocal laser scanning microscopy[24].
861 Fourth, calibration of the amount of DNA represented by each SMP in a given
862 section allows estimates of the absolute DNA density of a given chromatin ensemble,
863 recorded in this section. For this purpose, it is necessary to count the number of SMPs
864 attributed to such an ensemble. This is easy in cases, where the outline of an ensemble
865 can be precisely determined, for example after FISH of DNA targets with specific
866 probes[31,106]. In the absence of further information, however, demarcation of individual
867 ensembles, say a chromatin loop, a chromatin domain, or a chromosome territory, from
868 neighboring structures, is difficult and often impossible. Using a customized version of
869 a published Voronoi algorithm[37], we dissected the cloud of SMPs into Voronoi areas
870 limited by lines with equal distances to neighboring SMPs. The smaller the distances
871 between neighboring SMPs, the smaller were the defined Voronoi areas, and the
872 higher was the estimated density of SMPs. This approach was performed without any
873 density thresholding based on biological assumptions about chromatin ensembles with
874 specific structural or functional properties. Based on Voronoi area frequencies we
875 generated a histogram of the DNA density distribution across a given optical section.
876 Based on the calibration between the number of SMPs and the corresponding DNA
877 content, histograms of Voronoi area frequencies were converted into a color-coded
878 map of absolute DNA densities (Mbp/μm^3). However, this advantage was achieved at
879 a cost: Voronoi tessellation is particularly useful to detect local DNA densities, likely
880 corresponding to small nucleosome clusters, but fails to detect chromatin loops formed
881 by extended ~10 nm thick nucleosomal chains or naked DNA.

882 **3D-Structured Illumination Microscopy (SIM)**

883 Super-resolution imaging of fixed cell samples with 3D-SIM was performed on a
884 DeltaVision OMX V3 system (Applied Precision Imaging/GE Healthcare) equipped with
885 a 100x/1.40 NA PlanApo oil immersion objective (Olympus), Cascade II:512 EMCCD
886 cameras (Photometrics) with 405 and 488 nm diode lasers. 3D-SIM image stacks were
887 acquired with a z-distance of 125 nm and with 15 raw images per plane (5 phases, 3
888 angles). The raw data was then computationally reconstructed using Wiener filter
889 settings 0.002 and channel-specifically measured optical transfer functions (OTFs)
890 using the softWoRX 6.0 software package (Applied Precision) to obtain a super-
891 resolution 3D image stack with a lateral (xy) resolution of ~120 nm and an axial (z)
892 resolution of ~300 nm. The level of spherical aberration was minimized and matched
893 to the respective OTFs using immersion oil with different refractive indices (RI)[47].
894 Images from the different color channels were registered with alignment parameters
895 obtained from calibration measurements with 0.2 µm diameter TetraSpeck beads
896 (Invitrogen). The reconstruction process generates 32-bit data sets with the pixel
897 number doubled in the lateral axes, and the lateral pixel size halved from 80 nm to
898 40 nm in order to meet the Nyquist sampling criterion. To normalize all image stacks
899 for subsequent image processing and data analysis, the stack-specific mode gray
900 value (representing the peak of the background noise) was subtracted, negative values
901 discarded and finally the format converted to 16-bit composite tiff-stacks using a
902 custom-made script based on ImageJ (http://rsbweb.nih.gov/ij).

903

904 **Confocal microscopy of microinjected nanobeads**

905 For confocal microscopy of microinjected nanobeads, a laser scanning and a spinning
906 disk confocal microscope were used. The TCS SP5 DMI 6000 CS CLSM microscope
907 (Leica Microsystems, Mannheim/Germany) was equipped with a HCX Plan

908 Apochromat Lambda Blue 63x/1.4 oil objective lens and various laser sources, the
909 excitation wavelengths ranging from 405 nm to 633 nm. Spinning disk confocal
910 microscopy was performed on an Ultraview system (PerkinElmer) equipped with
911 405 nm, 488 nm, and 561 nm diode lasers using a 100x/1.4 oil Apochromat (Zeiss)
912 objective lens.

913 **Electron Spectroscopic Imaging (ESI)**

914 C3H 10T1/2 growing in 35mm MatTek glass bottom dishes cells were fixed in 0.1 M
915 Phosphate Buffer containing 4% paraformaldehyde and 2% glutaraldehyde for 30 min.
916 Then the cells were permeabilized with 0.1% Triton X-100 for 15 min. After washing
917 with 1xPBS the cells were treated with RNAse as described above. After a dehydration
918 series (50%, 70%, 90%,100%) each 30 min, the cells were infiltrated with acrylic resin
919 (LR White) (1:1 mixture with 100% ethanol for 4h and in pure LR White overnight).
920 Placing an LR White filled 2 ml Eppendorf tube on top of the cells and polymerizing the
921 acrylic resin for 48h at 65°C in the oven, blocks were created that could after detaching
922 from the glass be trimmed and cut with a Diatome diamond knife on a Leica Ultracut
923 UC6 microtome[107]. 100 nm ultrathin sections were picked up on 300 Mesh copper grids
924 and carbon coated. Cells were located in a JEOL F2100 transmission electron
925 microscope. Phosphorous and nitrogen elemental maps were recorded using a
926 GATAN Quantum post column electron energy loss spectrometer equipped with a
927 GATAN UltraSCAN 1000 CCD camera. For phosphorous elemental maps, post-edge
928 pictures were recorded at 162.5 eV (slit width 20 eV) and pre-edge images at 119.5
929 eV and 99.5 eV (slit width 20 eV each) (3-window method). For nitrogen elemental
930 maps, post-edge pictures were recorded at 416 eV (slit width) and pre-edge pictures
931 were recorded at 416 eV and 383 eV (slit width 30 eV each). Phosphorous and nitrogen
932 elemental maps were computed in Digital Micrograph by GATAN.

933 **Supplementary Information**
934

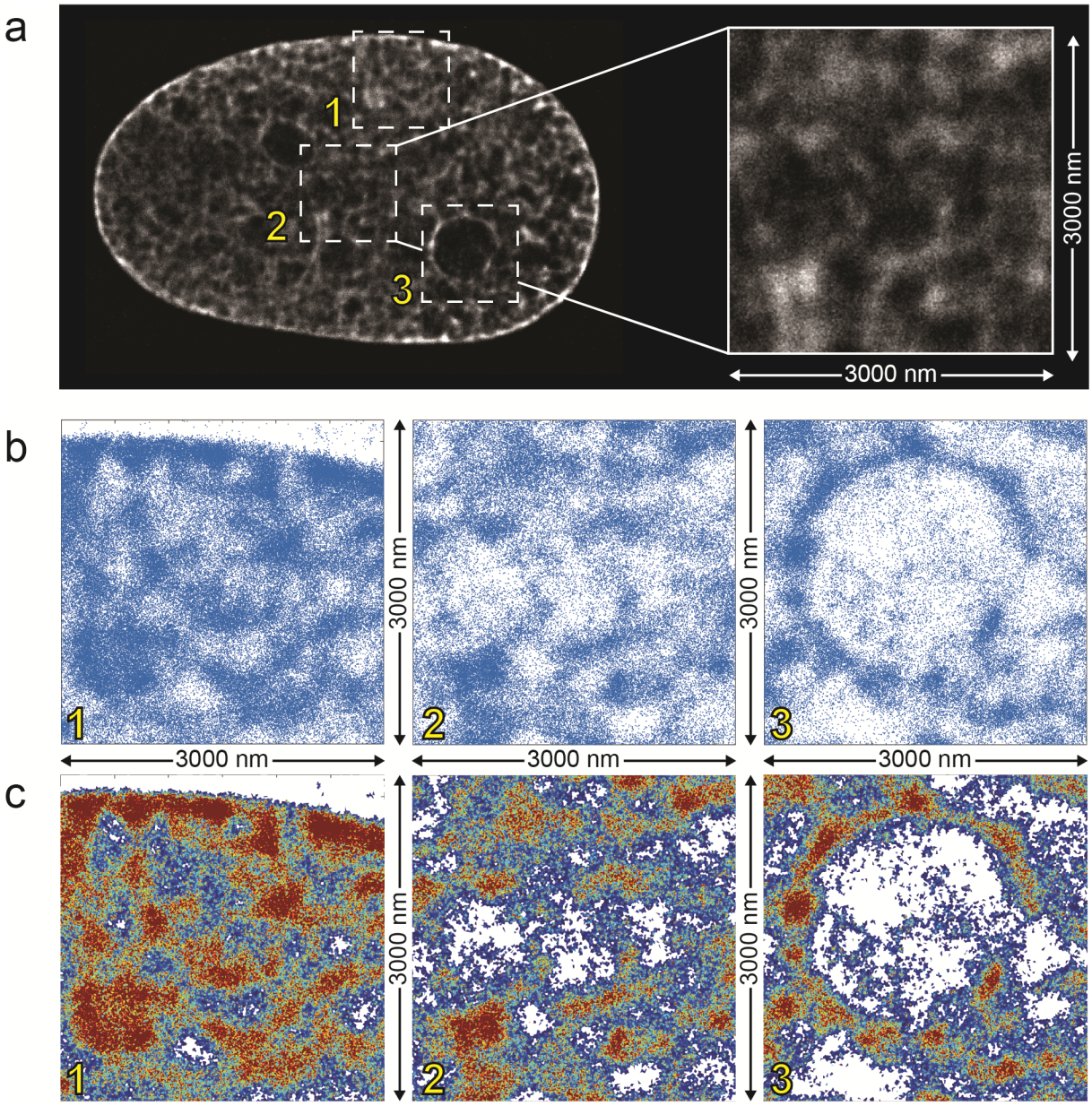

935
936 **Supplemental Figure S1**
937 **Processing of SMLM images and generation of high-resolution nuclear**
938 **landscapes**
939 ***a*** *SMLM-fBALM image of a mid-plane optical section through a BJ1 cell nucleus stained with*
940 *Sytox-Orange yielding about 10 million SMPs with a lateral structural resolution of about 20*
941 *nm and an axial resolution of about 600 nm. SMPs were binned in pixels with 10 nm edge*
942 *length. For this overview, a region was chosen with densely arranged SMPs corresponding to*
943 *the INC. The three boxes mark regions at the nuclear periphery (1), in the nuclear center (2)*
944 *and a nucleolus (3). Supplemental Video S1a shows a movie of the enlarged box 2 in (a) with*
945 *SMPs at increasing density and structural resolution; Supplemental Video S1b provides a view*
946 *on the rotating 600 nm thick section.* ***b, 1-3*** *Enlargements of boxes 1-3 represent 2D*
947 *localization maps of all individual SMPs in 100 nm thick optical subsections with an average*
948 *lateral localization precision of ca. 8 nm and ca. 50 nm along the optical axis (see Results for*
949 *explanation, how 100 nm thick subsections were achieved from the 600 nm thick primary*
950 *optical section).* ***c, 1-3*** *The same boxes as above are presented here after Voronoi-tessellation*
951 *as true-to-scale color-coded DNA density maps (Mbp/µm^3), compare DNA density scale bar in*

952 *Figure 2, where the identical panel is shown in Fig. 2b1-3. For calculations of 3D DNA densities*
953 *see Results*

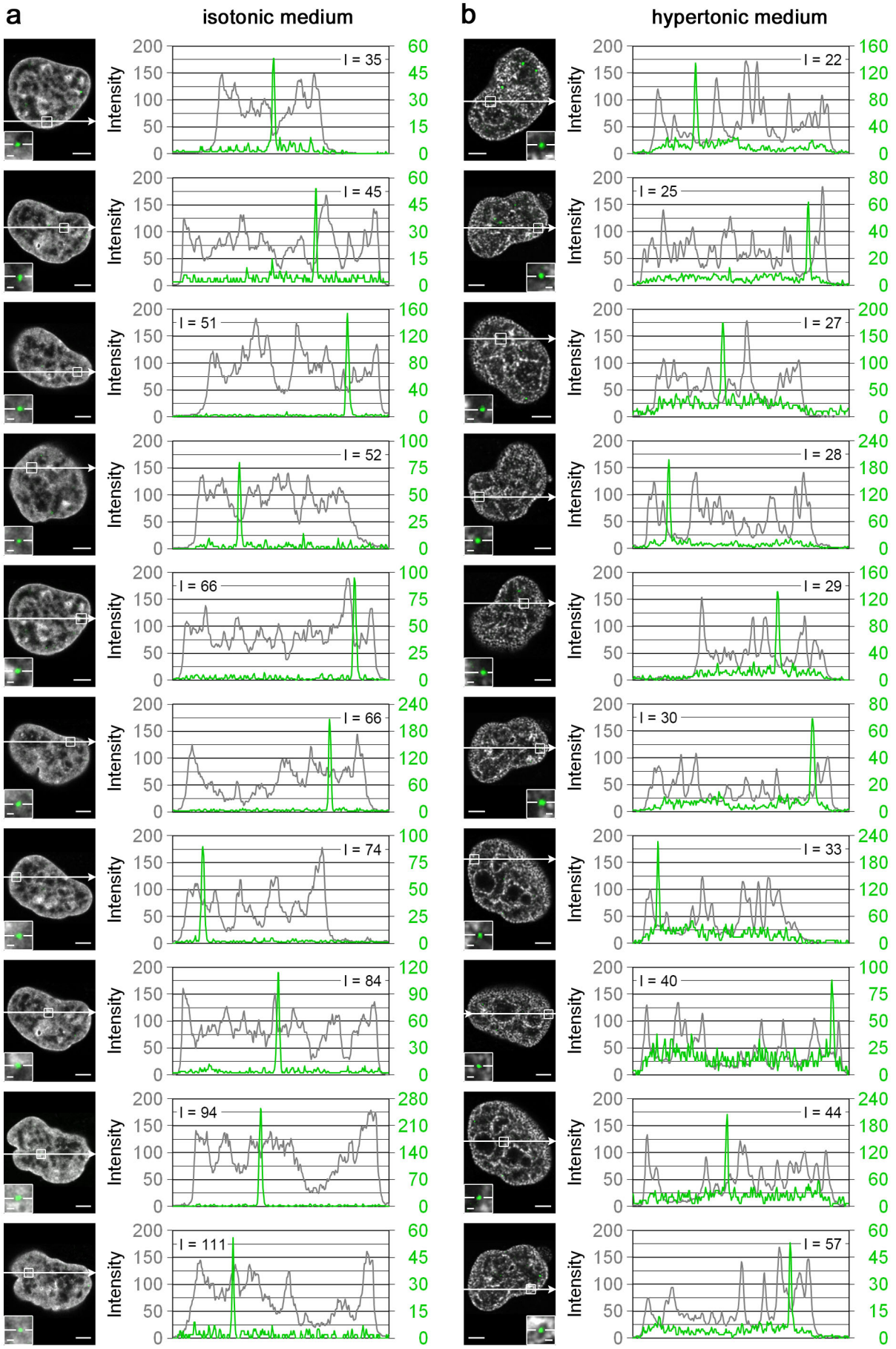

954

955
956 **Supplemental Figure S2**
957 *Localization of nanobeads (with 20 nm diameter) in nuclei of HeLa cells kept in* ***(a)*** *isotonic*
958 *medium with normally condensed chromatin (NCC) or* ***(b)*** *hypertonic medium with hyper-*
959 *condensed chromatin (HCC). The confocal sections (left columns in a and b) show the position*
960 *of the intensity line plotted at the right, the arrow denotes the scanning direction. The area of*
961 *the bead is magnified in the inset. Scale bars: 4 µm, 0.5 µm in insets. For each nucleus, line*
962 *scans were made through a given bead (green line) and through the normalized DAPI intensity*
963 *image (black line). The relative DNA density (I; grey values 0 - 255) present at the site of a*
964 *nanobead was determined in the confocal section with the brightest spot. Nanobeads are*
965 *localized within valleys of the DNA density landscape and sometimes at the slope of DNA*
966 *density peaks.*

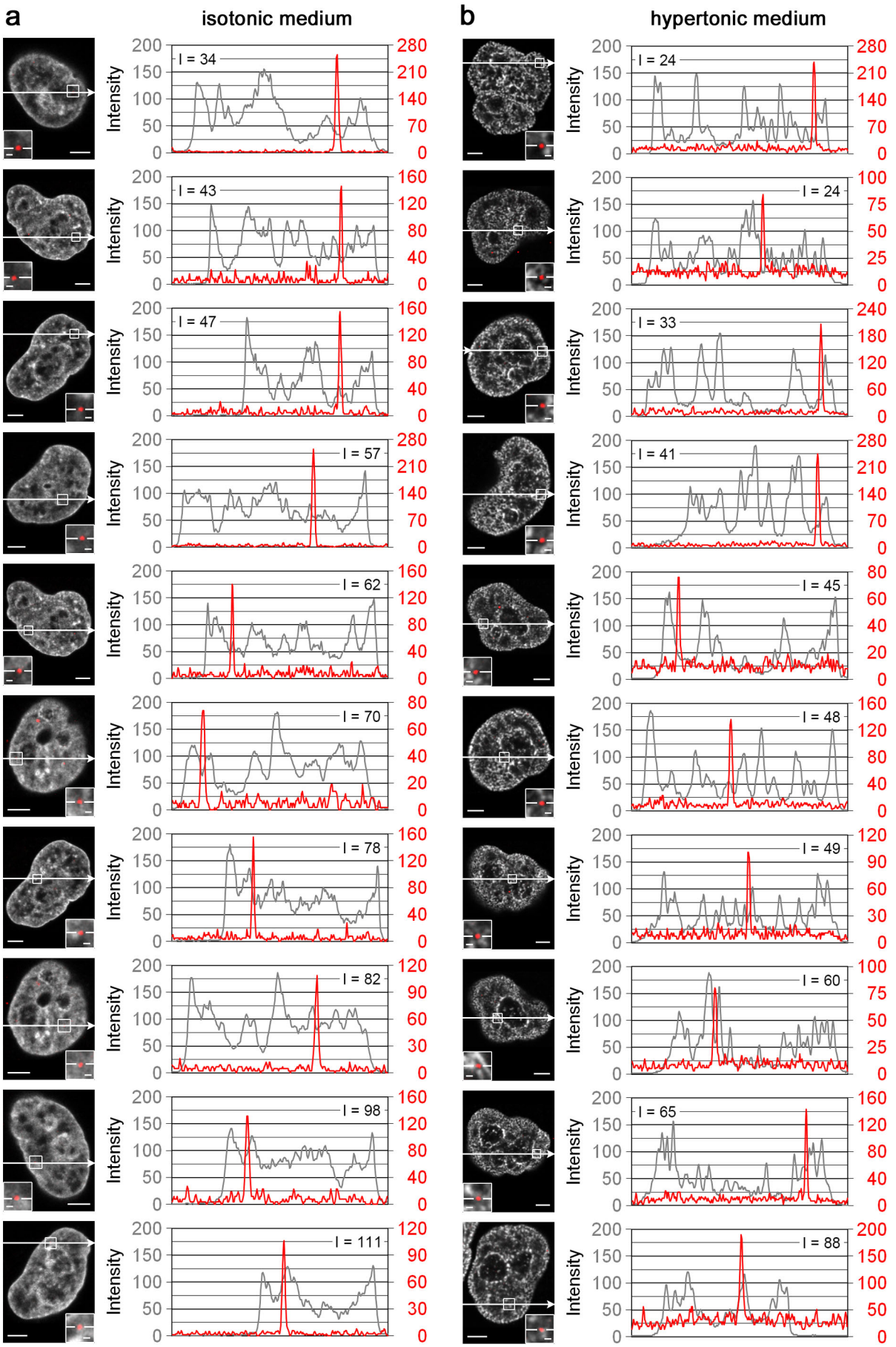
a
isotonic medium
b
hypertonic medium
Intensity
I = 34
I = 43
I = 47
I = 57
I = 62
I = 70
I = 78
I = 82
I = 98
I = 111
I = 24
I = 24
I = 33
I = 41
I = 45
I = 48
I = 49
I = 60
I = 65
I = 88

967

968 **Supplemental Figure S3**
969 *Localization of nanobeads (with 40 nm diameter) in nuclei of HeLa cells kept **(a)** in isotonic*
970 *medium with normally condensed chromatin (NCC) or **(b)** hypertonic medium with hyper-*
971 *condensed chromatin (HCC). Nanobeads are localized within valleys of the DNA density*
972 *landscape and sometimes at the slope of DNA density peaks. For further details see legend*
973 *to Supplemental Figure S2.*
974
975 **Supplemental Videos S1a and S1b**
976 *Movie with the positions of blinking signals (SMPs) recorded from DNA bound Sytox*
977 *orange molecules (SMPs) in the BJ1 nucleus shown in Figure 2. The SM positions of*
978 *a mid-plane optical section (thickness ~ 600 nm) of this BJ1-nucleus with about 10*
979 *million localizations were visualized by assigning each SM position to a 10 nm sized*
980 *pixel (corresponding to the average localization precision of 8.5 nm). **Video S1a** starts*
981 *with the visualization of the entire nuclear section and then zooms in to smaller regions*
982 *of interest (boxed area 2). **Video S1b** provides a view on the rotating 600 nm thick section.*
983
984 **Supplemental Video S2**
985 *Movie of a C3H 10T1/2 nucleus recorded for 6 hours after microinjection of three 20*
986 *nm sized nanobeads. Magnified images of two nanobeads in the 'lower' part of the*
987 *nucleus are shown in Figure 5f,g. Other nanobeads or clusters were located in the*
988 *cytoplasm, as demonstrated by serial sections. The display on the left shows the*
989 *moving, intranuclear nanobeads. Notably, movements of nanobeads in the cytoplasm*
990 *were more rapid and extensive. The right display demonstrates a random-walk like*
991 *trajectories of intranuclear nanobeads (compare Figure 5h).*
992
993
994 **References**
995

996 1 Gasser, S. M. & Laemmli, U. A glimpse at chromosomal order. *Trends in Genetics* **3**, 16-
997 22 (1987).
998 2 Cremer, T. *et al.* The Interchromatin Compartment Participates in the Structural and
999 Functional Organization of the Cell Nucleus. *Bioessays* **42**, e1900132,
1000 doi:10.1002/bies.201900132 (2020).
1001 3 Cremer, T. *et al.* The 4D nucleome: Evidence for a dynamic nuclear landscape based
1002 on co-aligned active and inactive nuclear compartments. *FEBS Lett* **589**, 2931-2943,
1003 doi:10.1016/j.febslet.2015.05.037 (2015).
1004 4 Maslova, A. & Krasikova, A. FISH Going Meso-Scale: A Microscopic Search for
1005 Chromatin Domains. *Front Cell Dev Biol* **9**, 753097, doi:10.3389/fcell.2021.753097
1006 (2021).
1007 5 Strickfaden, H. Reflections on the organization and the physical state of chromatin in
1008 eukaryotic cells. *Genome* **64**, 311-325, doi:10.1139/gen-2020-0132 (2021).
1009 6 Dekker, J. *et al.* The 4D nucleome project. *Nature* **549**, 219-226,
1010 doi:10.1038/nature23884 (2017).
1011 7 Di Stefano, M., Paulsen, J., Lien, T. G., Hovig, E. & Micheletti, C. Hi-C-constrained
1012 physical models of human chromosomes recover functionally-related properties of
1013 genome organization. *Sci Rep* **6**, 35985, doi:10.1038/srep35985 (2016).
1014 8 Kempfer, R. & Pombo, A. Methods for mapping 3D chromosome architecture. *Nat Rev*
1015 *Genet* **21**, 207-226, doi:10.1038/s41576-019-0195-2 (2020).
1016 9 Moretti, C., Stevant, I. & Ghavi-Helm, Y. 3D genome organisation in Drosophila. *Brief*
1017 *Funct Genomics* **19**, 92-100, doi:10.1093/bfgp/elz029 (2020).
1018 10 Cremer, M. *et al.* Cohesin depleted cells rebuild functional nuclear compartments after
1019 endomitosis. *Nat Commun* **11**, 6146, doi:10.1038/s41467-020-19876-6 (2020).
1020 11 Belmont, A. S. Nuclear Compartments: An Incomplete Primer to Nuclear
1021 Compartments, Bodies, and Genome Organization Relative to Nuclear Architecture.
1022 *Cold Spring Harb Perspect Biol*, doi:10.1101/cshperspect.a041268 (2021).

12 Misteli, T. The Self-Organizing Genome: Principles of Genome Architecture and Function. *Cell* **183**, 28-45, doi:10.1016/j.cell.2020.09.014 (2020).
13 Cardozo Gizzi, A. M. A Shift in Paradigms: Spatial Genomics Approaches to Reveal Single-Cell Principles of Genome Organization. *Front. Genet.* **Article 780822**, doi:https://doi.org/10.3389/fgene.2021.780822 (2021).
14 Kamat, K., Qi, Y., Wang, Y., Ma, J. & Zhang, B. Genome Compartmentalization with Nuclear Landmarks: Random yet Precise. *bioRxiv preprint*, doi:https://doi.org/10.1101/2021.11.12.468401 (2021).
15 Sood, V. & Misteli, T. The stochastic nature of genome organization and function. *Curr Opin Genet Dev* **72**, 45-52, doi:10.1016/j.gde.2021.10.004 (2021).
16 Maeshima, K. *et al.* The physical size of transcription factors is key to transcriptional regulation in chromatin domains. *J Phys Condens Matter* **27**, 064116, doi:10.1088/0953-8984/27/6/064116 (2015).
17 Cremer, T. & Cremer, M. Chromosome territories. *Cold Spring Harb Perspect Biol* **2**, a003889, doi:10.1101/cshperspect.a003889 (2010).
18 Paulsen, J., Liyakat Ali, T. M. & Collas, P. Computational 3D genome modeling using Chrom3D. *Nat Protoc* **13**, 1137-1152, doi:10.1038/nprot.2018.009 (2018).
19 Babokhov, M., Hibino, K., Itoh, Y. & Maeshima, K. Local Chromatin Motion and Transcription. *J Mol Biol* **432**, 694-700, doi:10.1016/j.jmb.2019.10.018 (2020).
20 Ricci, M. A., Manzo, C., Garcia-Parajo, M. F., Lakadamyali, M. & Cosma, M. P. Chromatin fibers are formed by heterogeneous groups of nucleosomes in vivo. *Cell* **160**, 1145-1158, doi:10.1016/j.cell.2015.01.054 (2015).
21 Gorisch, S. M., Richter, K., Scheuermann, M. O., Herrmann, H. & Lichter, P. Diffusion-limited compartmentalization of mammalian cell nuclei assessed by microinjected macromolecules. *Exp Cell Res* **289**, 282-294, doi:10.1016/s0014-4827(03)00265-9 (2003).
22 Lenart, P. *et al.* Nuclear envelope breakdown in starfish oocytes proceeds by partial NPC disassembly followed by a rapidly spreading fenestration of nuclear membranes. *J Cell Biol* **160**, 1055-1068, doi:10.1083/jcb.200211076 (2003).
23 Verschure, P. J. *et al.* Condensed chromatin domains in the mammalian nucleus are accessible to large macromolecules. *EMBO Rep* **4**, 861-866, doi:10.1038/sj.embor.embor922 (2003).
24 Weidemann, T. *et al.* Counting nucleosomes in living cells with a combination of fluorescence correlation spectroscopy and confocal imaging. *J Mol Biol* **334**, 229-240, doi:10.1016/j.jmb.2003.08.063 (2003).
25 Imai, R. *et al.* Density imaging of heterochromatin in live cells using orientation-independent-DIC microscopy. *Mol Biol Cell* **28**, 3349-3359, doi:10.1091/mbc.E17-06-0359 (2017).
26 Cremer, C. & Masters, B. R. Resolution enhancement techniques in microscopy. *The European Physical Journal H* **38**, 281-344, doi:10.1140/epjh/e2012-20060-1 (2013).
27 Gould, T. J. & Bewersdorf, J. Nanoscopy at low light intensities shows its potential. *Elife* **1**, e00475, doi:10.7554/eLife.00475 (2012).
28 Khater, I. M., Nabi, I. R. & Hamarneh, G. A Review of Super-Resolution Single-Molecule Localization Microscopy Cluster Analysis and Quantification Methods. *Patterns (N Y)* **1**, 100038, doi:10.1016/j.patter.2020.100038 (2020).
29 Lelek, M. *et al.* Single-molecule localization microscopy. *Nat Rev Methods Primers* **1**, doi:https://doi.org/10.1038/s43586-021-00038-x (2021).
30 Schermelleh, L. *et al.* Super-resolution microscopy demystified. *Nat Cell Biol* **21**, 72-84, doi:10.1038/s41556-018-0251-8 (2019).
31 Bintu, B. *et al.* Super-resolution chromatin tracing reveals domains and cooperative interactions in single cells. *Science* **362**, doi:10.1126/science.aau1783 (2018).
32 Szabo, Q., Bantignies, F. & Cavalli, G. Principles of genome folding into topologically associating domains. *Sci Adv* **5**, eaaw1668, doi:10.1126/sciadv.aaw1668 (2019).
33 Szabo, Q. *et al.* TADs are 3D structural units of higher-order chromosome organization in Drosophila. *Sci Adv* **4**, eaar8082, doi:10.1126/sciadv.aar8082 (2018).
34 Cremer, C., Szczurek, A., Schock, F., Gourram, A. & Birk, U. Super-resolution microscopy approaches to nuclear nanostructure imaging. *Methods* **123**, 11-32, doi:10.1016/j.ymeth.2017.03.019 (2017).

35 Szczurek, A. *et al.* Super-resolution binding activated localization microscopy through reversible change of DNA conformation. *Nucleus* **9**, 182-189, doi:10.1080/19491034.2017.1419846 (2018).
36 Szczurek, A. *et al.* Imaging chromatin nanostructure with binding-activated localization microscopy based on DNA structure fluctuations. *Nucleic Acids Res* **45**, e56, doi:10.1093/nar/gkw1301 (2017).
37 Andronov, L., Orlov, I., Lutz, Y., Vonesch, J. L. & Klaholz, B. P. ClusterViSu, a method for clustering of protein complexes by Voronoi tessellation in super-resolution microscopy. *Sci Rep* **6**, 24084, doi:10.1038/srep24084 (2016).
38 Hendzel, M. J. & Bazett-Jones, D. P. Probing nuclear ultrastructure by electron spectroscopic imaging. *J Microsc* **182**, 1-14, doi:10.1046/j.1365-2818.1996.123403.x (1996).
39 Albiez, H. *et al.* Chromatin domains and the interchromatin compartment form structurally defined and functionally interacting nuclear networks. *Chromosome Res* **14**, 707-733, doi:10.1007/s10577-006-1086-x (2006).
40 Hübner, B. Functional nuclear architecture in normal cells and after manipulation of the nuclear landscape. Dissertation, LMU München: Faculty of Biology *Thesis, (Dissertation, LMU Munich)*, doi:10.5282/edoc.27814 (2020).
41 Wolff, H. *et al.* Analysis of the influence of subcellular localization of the HIV Rev protein on Rev-dependent gene expression by multi-fluorescence live-cell imaging. *Exp Cell Res* **312**, 443-456, doi:10.1016/j.yexcr.2005.11.020 (2006).
42 Strickfaden, H., Zunhammer, A., van Koningsbruggen, S., Kohler, D. & Cremer, T. 4D chromatin dynamics in cycling cells: Theodor Boveri's hypotheses revisited. *Nucleus* **1**, 284-297, doi:10.4161/nucl.1.3.11969 (2010).
43 Hell, S. & Stelzer, E. H. K. Properties of a 4Pi confocal fluorescence microscope. *J. Opt. Soc. Am. A* **9**, 2159-2166, doi:10.1364/JOSAA.9.002159 (1992).
44 Meggendorfer, M., Weierich, C., Wolff, H., Brack-Werner, R. & Cremer, T. Functional nuclear topography of transcriptionally inducible extra-chromosomal transgene clusters. *Chromosome Res* **18**, 401-417, doi:10.1007/s10577-010-9133-z (2010).
45 Kirmes, I. *et al.* A transient ischemic environment induces reversible compaction of chromatin. *Genome Biol* **16**, 246, doi:10.1186/s13059-015-0802-2 (2015).
46 Miron, E. *et al.* Chromatin arranges in chains of mesoscale domains with nanoscale functional topography independent of cohesin. *Science Advances* **6**, eaba8811, doi:DOI: 10.1126/sciadv.aba8811 (2020).
47 Smeets, D. *et al.* Three-dimensional super-resolution microscopy of the inactive X chromosome territory reveals a collapse of its active nuclear compartment harboring distinct Xist RNA foci. *Epigenetics Chromatin* **7**, 8, doi:10.1186/1756-8935-7-8 (2014).
48 Rouquette, J., Cremer, C., Cremer, T. & Fakan, S. Functional nuclear architecture studied by microscopy: present and future. *Int Rev Cell Mol Biol* **282**, 1-90, doi:10.1016/S1937-6448(10)82001-5 (2010).
49 Leidescher, S. *et al.* Spatial organization of transcribed eukaryotic genes. *Nature Cell Biology* **in pres**, doi: (2022).
50 Solovei, I. *et al.* Topology of double minutes (dmins) and homogeneously staining regions (HSRs) in nuclei of human neuroblastoma cell lines. *Genes Chromosomes Cancer* **29**, 297-308, doi:10.1002/1098-2264(2000)9999:9999<::aid-gcc1046>3.0.co;2-h (2000).
51 Cremer, M. & Cremer, T. Nuclear compartmentalization, dynamics, and function of regulatory DNA sequences. *Genes Chromosomes Cancer* **58**, 427-436, doi:10.1002/gcc.22714 (2019).
52 Horikoshi, Y. *et al.* Distinctive nuclear zone for RAD51-mediated homologous recombinational DNA repair. *bioRxiv preprint*, doi:DOI: 10.1101/2021.11.29.470307 (2021).
53 Lopez Perez, R. *et al.* Superresolution light microscopy shows nanostructure of carbon ion radiation-induced DNA double-strand break repair foci. *FASEB J* **30**, 2767-2776, doi:10.1096/fj.201500106R (2016).
54 Zakirov, A. N. *et al.* Fiber-Like Organization as a Basic Principle for Euchromatin Higher-Order Structure. *Front. Cell Dev. Biol.* **9**, 784440, doi:doi: 10.3389/fcell.2021.784440 (2022).

55 Sureka, R. & Mishra, R. Identification of Evolutionarily Conserved Nuclear Matrix Proteins and Their Prokaryotic Origins. *J Proteome Res* **20**, 518-530, doi:10.1021/acs.jproteome.0c00550 (2021).
56 Farabella, I., Di Stefano, M., Soler-Vila, P., Marti-Marimon, M. & Marti-Renom, M. A. Three-dimensional genome organization via triplex-forming RNAs. *Nat Struct Mol Biol* **28**, 945-954, doi:10.1038/s41594-021-00678-3 (2021).
57 Razin, S. V. & Gavrilov, A. A. Non-coding RNAs in chromatin folding and nuclear organization. *Cell Mol Life Sci* **78**, 5489-5504, doi:10.1007/s00018-021-03876-w (2021).
58 Eltsov, M., Maclellan, K. M., Maeshima, K., Frangakis, A. S. & Dubochet, J. Analysis of cryo-electron microscopy images does not support the existence of 30-nm chromatin fibers in mitotic chromosomes in situ. *Proc Natl Acad Sci U S A* **105**, 19732-19737, doi:10.1073/pnas.0810057105 (2008).
59 Beagrie, R. A. *et al.* Multiplex-GAM: genome-wide identification of chromatin contacts yields insights not captured by Hi-C *bioRxiv*, doi:https://doi.org/10.1101/2020.07.31.230284 (2021).
60 Jerkovic, I. & Cavalli, G. Understanding 3D genome organization by multidisciplinary methods. *Nat Rev Mol Cell Biol* **22**, 511-528, doi:10.1038/s41580-021-00362-w (2021).
61 Minnoye, L. *et al.* Chromatin accessibility profiling methods. *Nature Reviews Methods Primers* **1**, doi:https://doi.org/10.1038/s43586-020-00008-9 (2021).
62 Hansen, J. C., Maeshima, K. & Hendzel, M. J. The solid and liquid states of chromatin. *Epigenetics Chromatin* **14**, 50, doi:10.1186/s13072-021-00424-5 (2021).
63 Strickfaden, H. *et al.* Condensed Chromatin Behaves like a Solid on the Mesoscale In Vitro and in Living Cells. *Cell* **183**, 1772-1784 e1713, doi:10.1016/j.cell.2020.11.027 (2020).
64 Rowley, M. J. & Corces, V. G. Organizational principles of 3D genome architecture. *Nat Rev Genet* **19**, 789-800, doi:10.1038/s41576-018-0060-8 (2018).
65 Cai, L., Panyukov, s. & Rubinstein, M. Hopping Diffusion of Nanoparticles in Polymer Matrices. *Macromolecules* **48**, 847-862, doi:DOI: 10.1021/ma501608x (2015).
66 Pluen, A., Netti, P. A., Jain, R. K. & Berk, D. A. Diffusion of macromolecules in agarose gels: comparison of linear and globular configurations. *Biophys J* **77**, 542-552, doi:10.1016/S0006-3495(99)76911-0 (1999).
67 Seelbinder, B. *et al.* Non-invasive Chromatin Deformation and Measurement of Differential Mechanical Properties in the Nucleus. *BioRxiv preprint*, doi:https://doi.org/10.1101/2021.12.15.472786 (2021).
68 Amiad-Pavlov, D. *et al.* Live imaging of chromatin distribution reveals novel principles of nuclear architecture and chromatin compartmentalization. *Sci Adv* **7**, doi:10.1126/sciadv.abf6251 (2021).
69 Bajpai, G., Amiad Pavlov, D., Lorber, D., Volk, T. & Safran, S. Mesoscale phase separation of chromatin in the nucleus. *Elife* **10**, doi:10.7554/eLife.63976 (2021).
70 Schmid, V. J., Cremer, M. & Cremer, T. Quantitative analyses of the 3D nuclear landscape recorded with super-resolved fluorescence microscopy. *Methods* **123**, 33-46, doi:10.1016/j.ymeth.2017.03.013 (2017).
71 Chiariello, A. M., Annunziatella, C., Bianco, S., Esposito, A. & Nicodemi, M. Polymer physics of chromosome large-scale 3D organisation. *Sci Rep* **6**, 29775, doi:10.1038/srep29775 (2016).
72 Bascom, G. D., Sanbonmatsu, K. Y. & Schlick, T. Mesoscale Modeling Reveals Hierarchical Looping of Chromatin Fibers Near Gene Regulatory Elements. *J Phys Chem B* **120**, 8642-8653, doi:10.1021/acs.jpcb.6b03197 (2016).
73 Odenheimer, J., Heermann, D. W. & Kreth, G. Brownian dynamics simulations reveal regulatory properties of higher-order chromatin structures. *Eur Biophys J* **38**, 749-756, doi:10.1007/s00249-009-0486-1 (2009).
74 Rosa, A. & Zimmer, C. Computational models of large-scale genome architecture. *Int Rev Cell Mol Biol* **307**, 275-349, doi:10.1016/B978-0-12-800046-5.00009-6 (2014).
75 Bascom, G. D., Myers, C. G. & Schlick, T. Mesoscale modeling reveals formation of an epigenetically driven HOXC gene hub. *Proc Natl Acad Sci U S A* **116**, 4955-4962, doi:10.1073/pnas.1816424116 (2019).

76 Cremer, T. *et al.* Chromosome Territories, Interchromatin Domain Compartment, and Nuclear Matrix: An Integrated View of the Functional Nuclear Architecture. *Critical reviews in Eukaryotic Gene Expression 10: 179-212* **10**, 179-212, doi:10.1615/CritRevEukarGeneExpr.v10.i2.60 (2000).
77 Baldi, S., Korber, P. & Becker, P. B. Beads on a string-nucleosome array arrangements and folding of the chromatin fiber. *Nat Struct Mol Biol* **27**, 109-118, doi:10.1038/s41594-019-0368-x (2020).
78 Kharerin, H., Bhat, P. J. & Padinhateeri, R. Role of nucleosome positioning in 3D chromatin organization and loop formation. *J Biosci* **45** (2020).
79 Markaki, Y., Smeets, D., Cremer, M. & Schermelleh, L. Fluorescence in situ hybridization applications for super-resolution 3D structured illumination microscopy. *Methods Mol Biol* **950**, 43-64, doi:10.1007/978-1-62703-137-0_4 (2013).
80 Markaki, Y. *et al.* The potential of 3D-FISH and super-resolution structured illumination microscopy for studies of 3D nuclear architecture: 3D structured illumination microscopy of defined chromosomal structures visualized by 3D (immuno)-FISH opens new perspectives for studies of nuclear architecture. *Bioessays* **34**, 412-426, doi:10.1002/bies.201100176 (2012).
81 Chu, L. A. *et al.* 5D superresolution imaging for a live cell nucleus. *Curr Opin Genet Dev* **67**, 77-83, doi:10.1016/j.gde.2020.11.005 (2021).
82 Shechtman, Y. *et al.* Observation of live chromatin dynamics in cells via 3D localization microscopy using Tetrapod point spread functions. *Biomed Opt Express* **8**, 5735-5748, doi:10.1364/BOE.8.005735 (2017).
83 Wombacher, R. *et al.* Live-cell super-resolution imaging with trimethoprim conjugates. *Nat Methods* **7**, 717-719, doi:10.1038/nmeth.1489 (2010).
84 Xiang, W. *et al.* Correlative live and super-resolution imaging reveals the dynamic structure of replication domains. *J Cell Biol* **217**, 1973-1984, doi:10.1083/jcb.201709074 (2018).
85 Branco, M. R. & Pombo, A. Intermingling of chromosome territories in interphase suggests role in translocations and transcription-dependent associations. *PLoS Biol* **4**, e138, doi:10.1371/journal.pbio.0040138 (2006).
86 Barth, R., Bystricky, K. & Shaban, H. A. Coupling chromatin structure and dynamics by live super-resolution imaging. *Sci Adv* **6**, doi:10.1126/sciadv.aaz2196 (2020).
87 Ma, H. *et al.* CRISPR-Cas9 nuclear dynamics and target recognition in living cells. *J Cell Biol* **214**, 529-537, doi:10.1083/jcb.201604115 (2016).
88 Gorkin, D. U. *et al.* An atlas of dynamic chromatin landscapes in mouse fetal development. *Nature* **583**, 744-751, doi:10.1038/s41586-020-2093-3 (2020).
89 Lohoff, T. *et al.* Integration of spatial and single-cell transcriptomic data elucidates mouse organogenesis. *Nat Biotechnol*, doi:10.1038/s41587-021-01006-2 (2021).
90 Yang, K. D. *et al.* Multi-domain translation between single-cell imaging and sequencing data using autoencoders. *Nat Commun* **12**, 31, doi:10.1038/s41467-020-20249-2 (2021).
91 Snyder, M. P. *et al.* The human body at cellular resolution: the NIH Human Biomolecular Atlas Program. *Nature* **574**, 187-192, doi:10.1038/s41586-019-1629-x (2019).
92 Cremer, T., Cremer, M. & Cremer, C. The 4D Nucleome: Genome Compartmentalization in an Evolutionary Context. *Biochemistry (Mosc)* **83**, 313-325, doi:10.1134/S000629791804003X (2018).
93 Simakov, O. *et al.* Deeply conserved synteny and the evolution of metazoan chromosomes. *Sci Adv* **8**, eabi5884, doi:10.1126/sciadv.abi5884 (2022).
94 Swygert, S. G. *et al.* Local chromatin fiber folding represses transcription and loop extrusion in quiescent cells. *Elife* **10**, doi:10.7554/eLife.72062 (2021).
95 Cremer, M. *et al.* Inheritance of gene density-related higher order chromatin arrangements in normal and tumor cell nuclei. *J Cell Biol* **162**, 809-820, doi:10.1083/jcb.200304096 (2003).
96 Bairstow, F. & Heidelberger, C. Increased thymidine uptake by methylcholanthrene-treated C3H/10T1/2 cells. *Int J Cancer* **16**, 370-375, doi:10.1002/ijc.2910160303 (1975).

97 Roukos, V., Pegoraro, G., Voss, T. C. & Misteli, T. Cell cycle staging of individual cells by fluorescence microscopy. *Nat Protoc* **10**, 334-348, doi:10.1038/nprot.2015.016 (2015).
98 Zurek-Biesiada, D. *et al.* Localization microscopy of DNA in situ using Vybrant((R)) DyeCycle Violet fluorescent probe: A new approach to study nuclear nanostructure at single molecule resolution. *Exp Cell Res* **343**, 97-106, doi:10.1016/j.yexcr.2015.08.020 (2016).
99 Amitai, A. & Holcman, D. Polymer physics of nuclear organization and function. *Physics Reports* **678**, 1-83, doi:doi.org/10.1016/j.physrep.2017.02.002 (2017).
100 Kaufmann, R. *et al. SPDM: single molecule superresolution of cellular nanostructures*. Vol. 7185 PWB (SPIE, 2009).
101 Chen, S.-Y., Bestvater, F., Schaufler, W., Heintzmann, R. & Cremer, C. Patterned illumination single molecule localization microscopy (piSMLM): user defined blinking regions of interest. *Opt. Express* **26**, 30009-30020, doi:10.1364/OE.26.030009 (2018).
102 Huang, B., Wang, W., Bates, M. & Zhuang, X. Three-dimensional super-resolution imaging by stochastic optical reconstruction microscopy. *Science* **319**, 810-813, doi:10.1126/science.1153529 (2008).
103 Reymann, J. *et al.* High-precision structural analysis of subnuclear complexes in fixed and live cells via spatially modulated illumination (SMI) microscopy. *Chromosome Res* **16**, 367-382, doi:10.1007/s10577-008-1238-2 (2008).
104 Chen, S. Y. Advanced Single Molecule Localization Microscopy for imaging cellular nuclei. . *Ph.D. Thesis, University Jena* (2020).
105 Chen, S. Y., Heintzmann, R. & Cremer, C. Sample drift estimation method based on speckle patterns formed by backscattered laser light. *Biomed Opt Express* **10**, 6462-6475, doi:10.1364/BOE.10.006462 (2019).
106 Weiland, Y., Lemmer, P. & Cremer, C. Combining FISH with localisation microscopy: Super-resolution imaging of nuclear genome nanostructures. *Chromosome Res* **19**, 5-23, doi:10.1007/s10577-010-9171-6 (2011).
107 Strickfaden, H., Xu, Z. Z. & Hendzel, M. J. Visualization of miniSOG Tagged DNA Repair Proteins in Combination with Electron Spectroscopic Imaging (ESI). *J Vis Exp*, doi:10.3791/52893 (2015).